Individual structural features constrain the functional connectome

Francesca Melozzi[1]*, Eyal Bergmann[2]*, Julie A. Harris[3], Itamar Kahn[2]**, Viktor Jirsa[1]**, Christophe Bernard[1]**

*Equal contribution first authors

**Equal contribution last authors

1. Aix Marseille Univ, Inserm, INS, Institut de Neurosciences des Systèmes, Marseille, France

2. Department of Neuroscience, Rappaport Faculty of Medicine, Technion – Israel Institute of Technology, Haifa, Israel

3. Allen Institute for Brain Science, Seattle, United States

Corresponding authors:

Christophe Bernard and Viktor Jirsa

christophe.bernard@univ-amu.fr ; viktor.jirsa@univ-amu.fr

Keywords: connectome, MRI, resting-state, large-scale models

ABSTRACT:

Whole brain dynamics intuitively depends upon the internal wiring of the brain; but to which extent the individual structural connectome constrains the corresponding functional connectome is unknown, even though its importance is uncontested. After acquiring structural data from individual mice, we virtualized their brain networks and simulated *in silico* functional MRI data. Theoretical results were validated against empirical awake functional MRI data obtained from the same mice. We demonstrate that individual structural connectomes predict the functional organization of individual brains. Using a virtual mouse brain derived from the Allen Mouse Brain Connectivity Atlas, we further show that the dominant predictors of individual structure-function relations are the asymmetry and the weights of the structural links. Model predictions were validated experimentally using tracer injections, identifying which missing connections (not measurable with diffusion MRI) are important for whole brain dynamics. Individual variations thus define a specific structural fingerprint with direct impact upon the functional organization of individual brains, a key feature for personalized medicine.

SIGNIFICANCE STATEMENT:

The structural connectome is a key determinant of brain function and dysfunction. The connectome-based model approach aims to understand the functional organization of the brain by modeling the brain as a dynamical system and then studying how the functional architecture rises from the underlying structural skeleton. Here, taking advantage of mice studies, we systematically investigated the informative content of different structural features in explaining the emergence of the functional ones. We demonstrate that individual variations define a specific structural fingerprint with a direct impact upon the functional organization of individual brains stressing the importance of using individualized models to understand brain function. We show how limitations of connectome reconstruction with the diffusion-MRI method restrict our comprehension of the structural-functional relation.

INTRODUCTION

Structural connectivity (SC) refers to set of physical links between brain areas (Connectome, (1)) and constitutes an individual fingerprint in humans (2, 3). Since the connectome provides the physical substrate for information flow in the brain, it should impose strong constraints on whole brain dynamics. Functional connectivity (FC), in the context of resting-state functional MRI, refers to coherent slow spontaneous fluctuations in the blood oxygenation level-dependent (BOLD) signals measured in the passive awake individual. FC is commonly used to assess whole brain dynamics and function (4). Similar to SC, FC constitutes an individual functional fingerprint (5–7), and shows specific alterations during aging and in brain disorders (8). There is thus a strong correlation between the structural and the functional connectome. However, the causal relation between SC and FC remains unknown. Large scale brain modeling offers a way to explore causality between structural and functional connectivity. Combining experimental and theoretical approaches, we here unravel and quantify the degree to which the individual's SC explains the same individual's variations in FC.

We use The Virtual Brain (TVB), which allows building individual brain network models based on structural data (9). This brain network modeling approach operationalizes the functional consequences of structural network variations (10, 11) and allows to systematically investigate SC-FC relations in individual human brains (12–15). If SC constrains FC, SC-based simulations of FC should match empirical FC within the bounds of validity of the metric. In primates and rodents, individual SCs are derived from diffusion MRI (dMRI). However, dMRI does not provide information on fiber directionality and suffers from limitations, such as underestimation of fiber length and misidentification of crossing fiber tracks (16, 17). Given the imprecision of dMRI derived SC, it is difficult to estimate the validity of the simulations. This would require the knowledge of the ground truth connectome of an individual, which cannot be measured at present. However, the currently best gold standard can be derived in mice from cellular-level tracing of axonal projections (18), here named the Allen connectome. Although individuality is lost (the SC is a composite of many mice) and despite other limitations (19, 20), the Allen connectome provides details not available otherwise and in particular not available in humans. Focusing our attention on simulating mouse brain dynamics, we can thus use this detailed connectome to explore which missing features in the dMRI account for individual SC-FC relations. Specifically, we predict that fiber directionality and fine grain connectivity patterns should be key determinants.

Using dMRI data of 19 mice, we constructed 19 virtual mouse brain models (21), and compared predicted FC with empirical FC data acquired from the same mice during passive wakefulness (22). We found that individual SC predicts individual FC better than the dMRI-based averaged SC, and that predictions can be improved by considering fiber directionality, coupling weights and specific fiber tracks derived from the Allen connectome. We also found that hemispherical lateralization in the mouse connectome influences whole brain dynamics.

RESULTS

We collected both dMRI and awake resting-state fMRI data (7 sessions per animal) from 19 hybrid B6/129P mice. We extracted SC from dMRI data to build individual virtual brains, which were imported into The Virtual Mouse Brain (TVMB), the extension of the open source neuroinformatic platform TVB (9) designed for accommodating large-scale simulations and analysis in the mouse, to generate *in silico* BOLD activity (21) using the reduced Wong Wang model (14, 23). We then compared simulated and empirical FC for each mouse in order to assess the power that an individual SC has to predict individual empirical FC derived from resting-state fMRI data (Figure 1). Further, SC was also obtained from the Allen connectome (our gold standard) in TVMB (21) to determine the contribution of information not available in dMRI-based SC. Experimental and simulated resting-state activity was characterized by a dynamical switching between stable functional configurations as revealed by the typical checkerboard patterns of Functional Connectivity Dynamics (FCD, Figure S1a and S1b), as observed previously (14, 24, 25). As expected, FCD varied across recording sessions (Figure S1b). In contrast, static Functional Connectivity (FC) was stable between experimental recording sessions (Figure 2A and Figure S1c). To compare the goodness of *in silico* resting-state dynamics against *in vivo* data, we needed a metric stable across experimental recording sessions in individual subjects, and thus we used the static FC for evaluating the Predictive Power (PP) of a SC.

We first defined the upper bound of the PP. The correlation value calculated between any pair of empirical FC for each mouse provides us with an upper boundary of the PP, taking into account inter-session variability and other sources of noise that preclude 100% PP accuracy (7, 26). In keeping with human data (6, 27), we found a high inter-session correlation for each of the 19 mice, demonstrating stability across different recording sessions in a given mouse (Figure 2A). Inter-session correlations within the same animal were greater than inter-subject correlations, indicating that there is an individual functional organization per mouse, which may act as a functional

fingerprint. Next, we sought to examine the extent to which individual functional connectomes correspond to individual structural connectomes.

SC obtained with a deterministic algorithm is a better predictor of FC

Here we considered probabilistic (Figure 2B) and deterministic (Figure 2C) dMRI-based SCs, using SD_Stream (28) and iFOD2 (29) within Mrtrix3 software (28) tractography algorithms, respectively. SC obtained with the deterministic algorithm yielded a greater PP than the SC obtained with the probabilistic one ($PP_{Individual-det} = 0.415 \pm 0.005$, $PP_{Individual-prob} = 0.392 \pm 0.005$, $mean \pm {}^{SD}/_{\sqrt{N}}$, Welch's test: $P < 0.001$ Figure 2E). The significative density difference in the two kind of connectomes ($Density_{Individual-prob} = 69 \pm 1\%$, $Density_{Individual-det} = 28.2 \pm 0.2\%$, Welch's test: $P < 0.001$), by itself, is not enough to explain the observed discrepancy in the PP. Connection density does not fully account for the predictive power of a connectome, but instead the relation depends on the connectome derivation (Figure S2). We argue that the observed difference in PP between deterministic and probabilistic processed connectomes depends on the proportion of false negative (FN) and false positive (FP) connections introduced by the two different algorithms: Zalesky and colleagues (2016)(30) show that the typical brain small-world topology is biased by the introduction of FP connections two times more than by the introduction of FN connections. In line with this finding, we attribute the difference in PP of the two connectomes to the detrimental role of FP connections, which are more likely introduced by probabilistic than deterministic tractography. However, deterministic tractography more likely overlooks some connections, introducing FN. This highlights the importance of preserving SC specificity (FN versus FP) versus SC sensitivity (FP versus FN) in the context of large-scale models. Namely, to preserve the global topology, specificity is more important as sensitivity in SC reconstruction. In the following, we compared deterministic SC-based simulated and empirical FCs.

Individual SC is the best predictor of individual FC

Next, we found that individual SCs had a greater predictive power than the averaged SC ($PP_{Individual-det} = 0.415 \pm 0.005$, $PP_{AVG-det} = 0.377 \pm 0.003$, Welch's test: $P < 0.001$, $PP_{Individual-prob} = 0.392 \pm 0.005$, $PP_{AVG-prob} = 0.349 \pm 0.004$, Welch's test: $P < 0.001$; Figure 2E), showing the importance of individual SCs. Although the Allen SC was obtained from hundreds of different mice, we found that it had a greater PP than individual dMRI-based SCs

($PP_{Individual-det} = 0.415 \pm 0.005$, $PP_{Tracer} = 0.488 \pm 0.005$, Welch's test: $P < 0.001$; Figure 2D,E), suggesting that the tracer-based connectome has structural information that is not present in dMRI, but which is central to explain the emergence of the functional connectome, even at the individual level. As the Allen SC was built from C57BL/6 mice, we verified the generality of our results in this strain (Figure S3a). Global signal regression, which improves structure-function relations and averaging recording sessions within each mouse (31), which reduces noise, increased the PP but did not alter the results (Figure S3b-c). Finally, splitting the recording sessions of each mouse, and submitting the data to a test-retest analysis revealed a close agreement between datasets (Figure S3d). Thus, our conclusions are strain- and preprocessing-independent, and reproducible.

Importance of long-range connections and directionality

To identify the source of the systematic superior performance of the Allen SC, we focused on the major limitations of dMRI: (1) difficulty to resolve long axonal tracts, (2) lack of information on fiber directionality and (3) imprecise estimation of connection weights. We estimated the contribution of fiber length by filtering the Allen SC to include only fibers present in the dMRI-based SC (Figure 3A); we characterized the role of fiber directionality by symmetrizing the Allen SC (Figure 3A), asymmetrizing the dMRI-based SC (Figure 3B), and quantifying the impact of each manipulation (Figure 3C).

Since dMRI fiber reconstruction reliability is inversely proportional to fiber length (16, 32, 33), dMRI SCs are sparser than the Allen SC (Figure 2B-C-D, S2a). To test the influence of the missing fibers in predicting FC, we built a filtered Allen SC (Figure 3A), which includes only the connections contained in at least one of the 19 deterministic dMRI SCs. The filtered connectome contains the 32% of the connections of the original tracer connectome, that are those captured by the dMRI-based deterministic processed connectomes. The connections that remain after the filtering operation are mainly those characterized by short-range length (Figure S2B): the averaged path length of the connections in the original and filtered tracer-based connectome is 5.40±0.02 mm and 3.57±0.03 mm, respectively (Welch's test, P<0.001). Figure 3C shows that the PP of the filtered Allen SC is lower than the original Allen SC ($PP_{Tracer\ filtered} = 0.461 \pm 0.005$, $PP_{Tracer} = 0.488 \pm 0.005$, Welch's test: $P < 0.001$; Figure 3C), however it remains statistically greater than the PP of individual SCs ($PP_{Individual-det} = 0.415 \pm 0.005$, Welch's test: $P < 0.001$; Figure 3C). Thus, although connections overlooked by the dMRI method, which are mainly long-range connections, are important to explain FC, other important structural features present in the Allen SC are

173 necessary to explain the discrepancy in PP between the tracer-based and dMRI-based connectomes.
174 We next focused on fiber directionality, since imposing bidirectional communication between
175 regions connected with unidirectional links *in vivo* may affect FC. We used an approach based on
176 surrogate SCs to test the role of directionality. Since the Allen SC contains directionality between
177 regions, we removed this information by symmetrizing it (Figure 3A). Figure 3C shows that
178 symmetrizing the Allen SC reduces its PP significantly ($PP_{Tracer\ sym} = 0.418 \pm 0.004$, $PP_{Tracer} =$
179 0.488 ± 0.005, Welch's test: $P < 0.001$; Figure 3C), making it comparable to the PP of the dMRI-
180 based SCs (Welch's test, $P < 0.001$). This demonstrates that directionality is a key determinant of
181 FC. It is notable that symmetrizing the filtered Allen SC led to a more modest reduction of the PP
182 than the symmetrisation of the original Allen SC ($PP_{Tracer\ sym} = 0.418 \pm 0.004$,
183 $PP_{Tracer\ filtered\ \&\ sym} = 0.446 \pm 0.004$, Welch's test: $P < 0.001$; Figure 3C). We argue that the PP
184 difference can be explained by considering the amount of false positive introduced in the surrogate
185 connectomes by the transformation: the filtering operation inserts FN connections, while the
186 symmetrisation operation inserts both FN and FP connections (34). It follows that the symmetrized
187 and filtered connectome contains less FP than just the symmetrized connectome. Thus, as
188 previously discussed for the tractography processing, introducing FP connections, as produced by
189 the symmetrisation but not by the filtering, is more detrimental than the introduction of FN
190 connections. To summarize when the tracer-based connectome is manipulated in order to remove
191 the information not detected by dMRI, which is the inability to detect (i) the directionality of brain
192 connections, as well as, (ii) some brain connections, especially the long-range ones, we found that
193 the removal of the directionality information biases the predictive power of the connectome more
194 than the removal of the connections not detected by the dMRI method.
195 We then took the complementary approach: enriching the dMRI-based SC with information on fiber
196 directionality, i.e. asymmetrizing it. The results show that asymmetrizing the dMRI SCs does not
197 increase, but rather decreases the PP ($PP_{Individual-det} = 0.415 \pm 0.005$, $PP_{Individual-det-asym} =$
198 0.394 ± 0.005, Welch's test: $P = 0.001$, $PP_{Individual-prob} = 0.392 \pm 0.005$,
199 $PP_{Individual-prob-asym} = 0.377 \pm 0.005$, Welch's test $P = 0.02$; Figure 3B,C). We argue that the
200 asymmetrization of the dMRI connectomes biased the PP because asymmetrizing a matrix is an ill-
201 posed problem, since there is no unique solution (more details can be found in the Methods). In
202 addition, there is no 1:1 correspondence between the connection strengths obtained with dMRI
203 (axonal bundles) and Allen ones (axonal branches) since axons tend to branch more or less profusely
204 when reaching their target zone.

205

206 **Connection strengths as key determinants of FC**

207 The symmetric filtered Allen SC and the deterministic dMRI SCs have a similar structure: both
208 matrices are symmetric and contain the same number of elements. Since the PP of the symmetric
209 filtered Allen SC is still greater than the dMRI one, the difference can only result from dissimilarities
210 in the values of the matrices' entries, i.e. the connection strength values. Figure 3D shows that there
211 is a significant relation between the normalized U-statistics of the Mann-Whitney test calculated
212 between the filtered symmetric Allen SC and the individual dMRI SC and the PP of the latter ($r =$
213 $0.52, P = 0.02$). Namely, the more the distribution of connection strengths of the deterministic
214 dMRI is similar to that of the Allen SC, the more reliable the predictions are. From the analysis of
215 the topological characteristics of the SCs, it emerges that there is a significant linear relation ($r =$
216 $-0.55, P = 0.014$; Figure S4d) between the PP of the deterministic dMRI SCs and the level of
217 topological organization of the connectome as a small world network, i.e. high local clustering yet
218 short average path (35) as measured by the Small World Propensity of a network (36). Specifically,
219 the more similar the network's connection topology of the dMRI SC is to the Allen one, the more
220 reliable the predictions are (Figure S4c-d).

221

222 **Specific refinement of individual dMRI connectomes**

223 Since some afferent and efferent connections of specific areas may not be reliably
224 reconstructed with dMRI, we examined whether refining dMRI SCs with more precise patterns
225 derived from the Allen SC would improve the PP. For each deterministic dMRI SC, we substituted
226 the non-zero incoming and outgoing connections of a specific region with the corresponding Allen
227 SC projections, thus building a *hybrid* connectome (Figure 4A, S5A).

228 When considering all mice, we found that substituting the anterior cingulate areas and the
229 right caudoputamen connectivity patterns with the Allen SC projections significantly improved the
230 PP of the connectome (left ACAd , improvement =0.047±0.006, t=7.23, P<0.001; left ACAv,
231 improvement 0.032±0.006, t=4.96, P=0.002; right ACAv, improvement=0.028±0.003, t=7.58,
232 P<0.001; right CP, improvement=0.018±0.003, t=6.42, $P < 0.001$; Figure 4B), suggesting that both
233 regions are poorly resolved by dMRI in mice. Importantly, the majority of substitutions decreased
234 the PP (Figure 4B). For each animal, we quantified the specificity of each connection with respect to
235 the other mice. Figure S5b shows that there is a relation between the connection specificity and the
236 change in PP when the corresponding connections are replaced with the non-specific tracer ones.

This result confirms that the specificity of connections in individuals is a key feature for brain dynamics.

For each individual SC, we identified the region in which replacement of its dMRI-connections with the Allen ones generates a new connectome, hybrid^{best}, which has the best PP improvement as compared to the other hybrid connectomes (Figure S5a). Figure 4C shows that the PP achieved by hybrid^{best} is statistically indistinguishable to the one achieved by the filtered Allen SC (Welch's test: $P = 0.95$). In other words, it is sufficient to replace in the dMRI SC the connections of one particular region with the corresponding Allen ones, to get a similar prediction, which is specific for each mouse.

The asymmetric mouse brain

Finally, we sought to estimate the potential contribution of asymmetric transhemispheric connectivity. Figure 4D shows that there is a considerable improvement in the PP of hybrid SCs when using connections from the right hemisphere, as compared to those from the left one. The Allen connections have been estimated using unilateral injection in the right hemisphere (18). Since no tracer injections were done in the left hemisphere, TVMB uses a mirror image of the right hemisphere to build the left one (21). This suggests that the tracer-based intra-hemispheric connectivity predicts better right intra-hemispheric functional behavior than the left one, as demonstrated in Figure S6a. Figure 4E shows that there is a significant relation between hemispheric lateralization in the functional connectomes and the improvement in PP when the right and left homotopic tracer area's connections are introduced in the dMRI SC ($r = 0.14, P = 0.01$). Namely, the more functional connections are asymmetric, the more the PP decreases when using the right hemisphere connections to build the left ones. These results suggest that connectivity asymmetry impacts brain dynamics and that it is region- and mouse-specific.

Hemispherical lateralization of the mouse brain

Figure 4E shows that the region demonstrating the greatest lateralization in terms of functional connectivity in individual mice is the supplemental somatosensory area (SSs). Figure 4B shows that when we introduce the mirror image of the right SSs into the dMRI SC, the predictive power is considerably decreased, which means that the mirror image of the right SSs poorly represents the true left SSs. We thus focused on the SSs area. If SC drives FC, we predicted that introducing in the tracer-based connectome the detailed left SSs connections, instead of using the

mirror image of the right SSs ones, would increase the PP of the connectome. We first performed tracer injections in the left SSs and determined the projection pattern. As predicted, we found evidence of an asymmetric distribution of fibers between the left and right SSs (Figure 5A). To test whether these structural differences were sufficient to explain the functional ones, we introduced the connections of the left SSs into the tracer connectome and obtained a statistically greater PP as compared to the ones of purely mirrored connectomes built from the injection experiments performed in the right SSs (Figure 5B). Next, we introduced the left connections of the SSs into the dMRI-based SCs (hybrid connectome), and, as predicted, we found a greater PP as compared to using the mirror image of the right connections of the SSs as shown in Figure 5C (between the 14 experiments performed in the right SSs we take into account the one whose injection location is more similar to those used in the left SSs injection experiment). Finally, since our previous results demonstrate that the lateralization is animal-dependent, we sought to examine whether lateralized FC is supported by lateralized SC, and found that the improvement of the PP following hybridization of left SSs dMRI connections is indeed proportional to the degree of functional lateralization ($r = 0.42, P = 0.01$; Figure 5D). Together, these results show that the mouse brain is structurally lateralized, and that this lateralization impacts whole brain dynamics at the individual subject-level.

DISCUSSION

Our results provide direct evidence of a type of causality between SC and FC, in the sense that individual structural connectomes predict their functional counterparts better than the dMRI-based averaged connectomes. Previous studies utilized the Allen Mouse Connectivity Atlas to study structure-function relations at the group level using voltage-sensitive dyes (37) and FC (22, 25, 38). In addition, a recent work in rats (39) used TVB to simulate FC based on SC and found strong correlation at the group level; a similar finding has been reported in humans (40). Here we compared structure-function relations in individual brains and we used the detailed Allen connectome as a gold standard to identify regions and connections that play a preeminent role in the emergence of individual brain dynamics. We showed that, similar to humans (6), intra-mice FCs are more stable than inter-mice FCs (Figure 2A). We propose that the emergence of the personal features in the functional data is, at least partially, driven by the emergence of underlying individual-specific structural organization with individual stable features (Figure 2E). Notwithstanding, we cannot

300 exclude that the variations in hemodynamic response functions (HRF) across animals and brain
301 location affect SC-FC relations, as it has been shown in humans (41). However, the fact that we
302 analyzed awake animals reduces the impact of this confounding factor (42, 43).

303 The detrimental role of false positive (FP) connections in the connectome topology has been
304 explored by (30) and (34) analyzing, respectively, the effect of FP as introduced by probabilistic
305 tractography and overlooking connections' directionality. In line with these findings, we showed
306 that the introduction of FP connections biases the connectome predictions. We found the dMRI-
307 based connectomes processed with the deterministic tractography have a statistically greater PP
308 than those processed with probabilistic algorithms. Since the observed difference in PP is not
309 directly related with the difference in connections density (Figure S2), we argue that the difference
310 in PP is driven by the different characteristics of the connections overlooked by both types of
311 tractography processing: more FP and less FN in the case of probabilistic processed connectivity,
312 and conversely in the case of deterministic processed connectivity. This highlights that brain
313 dynamics predictions are more accurate if connectome specificity is preserved, even at the cost of
314 sensitivity, as it is the case of deterministic processed connectome.

315 When processing the tracer-based data, the probabilistic computational model used to
316 construct the original Allen connectome (18) may introduce several false negative connections,
317 resulting in a low connection density reconstruction (35-73%), whilst others reported a 97% density
318 (19, 20). Here, we have used the Allen connectome builder interface, which implements a
319 deterministic approach to reconstruct whole brain connectivity (21), leading to a 98% density of
320 connections. Still, as shown in Figure 3B, the introduction of FN connections (filtered tracer-based
321 connectome) does not dramatically influence the PP of the connectome.

322 The main drawback of the Allen connectome is that it has been obtained from hundreds of
323 different mice, thus blurring individual variability. In keeping with this, we found that replacing most
324 individual dMRI connections with Allen connections reduces the PP. However, in some regions such
325 as the anterior cingulate and the caudoputamen, group-level Allen connections outperform
326 individual dMRI connections. This finding can be explained by the fact that connections from the
327 anterior cingulate are difficult to resolve as this area is located in the midline brain region, where
328 the cortex folds, resulting in an abrupt change in fiber directionality. Moreover, the axons make
329 sharp turns around the corpus callosum while the extraction algorithm assumes a logical
330 continuation of the vector direction. The connections of the striatum are often short and, due to its
331 multipolar organization without a clear gradient orientation limiting fiber reconstruction. To sum

332 up, including the tracer information of these complex fiber pathways in the dMRI-based
333 connectome significantly increases the predictive power of individual connectomes. It would be
334 interesting to test the same procedure when using whole brain modeling of human individuals by
335 including tracer information from non-human primates experiments.

336 Although the Allen connectome was obtained from C57BL/6 mice, brain dynamics of hybrid
337 F1 mice could be predicted by the Allen connectome, suggesting that the structural organization of
338 the mouse brain was not impacted by out-breeding. Findings from hybrid mice are considered more
339 generalizable to other strains (44), thus suggesting that the pattern observed here is not strain-
340 specific. Nonetheless, since the genetic background affects the behavioral phenotype (45), it will be
341 important to systematically assess these findings in mouse strains where this aspect is directly
342 manipulated.

343 The Allen SC includes directionality and long-range connections, which are not well (or at all)
344 resolved by dMRI. However, the removal of the connections not resolved by dMRI-based
345 connectomes, mostly those characterized by long-range length, is not sufficient to explain the
346 discrepancy between the tracer-based and dMRI-based predictive power. In addition, we showed
347 that removing the directionality information from the tracer-based connectome, that it is
348 symmetrizing the connectome, thus introducing FP and FN connections, worsens the predictive
349 power more than the filtering operation, that consist in introducing just FN connections (34). This
350 shows the key role of connections directionality in predicting brain dynamics; and it confirms our
351 results on tractography algorithm processing: FP connections biases the predictive power ability of
352 the connectome more than FN. Finally, analyzing the connections strength differences between the
353 dMRI and tracer-based connectome, we have showed that connection strengths are the main
354 determinant of these dynamics, and consequently of individuality (Figure 3D).

355 An unexpected result was the important role played by the transhemispheric asymmetry of
356 connections. This finding is consistent with calcium imaging studies reporting such asymmetry in
357 rodents (46). By comparing injections between left and right hemispheres, we confirmed our
358 prediction that the approximation of left areas connections as right areas' connections, necessary
359 in the tracer-based connectome reconstruction, significantly affect the predictive power of the
360 connectome. Moreover, we showed that the bias introduced by this approximation is proportional
361 to the degree of the individual animal's functional lateralization.

362 Progress in connectomics enabled the development of large-scale brain models to study brain
363 function in health and disease (12, 47). Although individual whole brain modelling has a potentially

high translational value for the benefit of patients (15, 48, 49), the entire approach relies on the extent to which individual differences in structural connectomes determine the emergent network dynamics and consequent neuroimaging signals. Although SC does not provide enough information to predict an epileptogenic zone in humans (50), our work shows that using more precise information (e.g. obtained from tracer injections in non-human primates) to take into account directionality, synaptic weights and poorly-resolved dMRI connections, will increase the predictive power. Our here demonstrated link of individual SC and FC variability and brain network modeling bears the promise to build a systematic approach to individual diagnosis and clinical decision making (15, 47).

MATERIALS AND METHODS

1.1. Animals and Surgical Procedures

All procedures were conducted in accordance with the ethical guidelines of the National Institutes of Health and were approved by the institutional animal care and use committee (IACUC) at Technion. 19 male first generation hybrid mice (B6129PF/J1, 9-12 weeks old) were implanted with MRI compatible head-posts using dental cement as previously described (22). After 3 days of recovery, the animals were acclimatized to extended head fixation. This training included 5 handling sessions performed over 3-5 days, and 4 daily acclimatization sessions inside the MRI scanner. In each acclimatization session, mice were briefly anesthetized with isoflurane (5%), and then head-fixed to a custom-made cradle for gradually longer periods (2, 5, 10, 25 min). Subsequently, mice underwent seven 45 min long awake imaging sessions, and one diffusion tensor imaging (DTI) session under continuous isoflurane anesthesia (0.5-1%). A second group that included 7 male inbred C57BL/6 mice (11-16 weeks old) was operated and scanned according to the same protocol. Experiments involving mice were approved by the Institutional Animal Care and Use Committees of the Allen Institute for Brain Science in accordance with NIH guidelines. For left side injections into SSs, surgical procedures were followed as described in (18). In brief, a pan-neuronal AAV expressing EGFP (rAAV2/1.hSynapsin.EGFP.WPRE.bGH, Penn Vector Core, AV-1-PV1696, Addgene ID 105539) was used for injections into wildtype C57BL/6J mice at postnatal day 56 (stock no. 00064, The Jackson Laboratory). SSs was targeted using stereotaxic coordinates from Bregma (AP: -0.7, ML, -3.4 and -3.9) and from brain surface (DV: 1.66). rAAV was delivered by iontophoresis with current settings of 3 µA at 7 s 'on' and 7 s 'off' cycles for 5 min total, using glass pipettes (inner tip diameters of 10–20 µm). Mice were perfused transcardially and brains collected 3 weeks post-injection for imaging using serial two-photon tomography, using methods as previously described for the Allen Mouse Connectivity Atlas (18).

1.2. *Data acquisition (fMRI and diffusion-MRI)*

MRI scans were performed at 9.4 Tesla MRI (Bruker BioSpin GmbH, Ettlingen, Germany) using a quadrature 86 mm transmit-only coil and a 20 mm loop receive-only coil (Bruker). Mice were shortly anesthetized (5% isoflurane) before mounted on the cradle. After acquisition of a short low-resolution rapid acquisition process with a relaxation enhancement (RARE) T1-weighted structural volume (TR = 1500 ms, TE = 8.5 ms, RARE-factor = 4, FA = 180°, 30 coronal slices, 150 × 150 × 450

404 μm^3 voxels, no interslice gap, FOV 19.2 × 19.2 mm^2, matrix size of 128 × 128), four spin echo EPI (SE-
405 EPI) runs measuring BOLD fluctuations were acquired (TR = 2500 ms, TE = 18.398 ms, 200 time
406 points, FA = 90°, 30 coronal slices, 150 × 150 × 450 μm^3 voxels, no interslice gap, FOV 14.4 × 9.6
407 mm^2, matrix size of 128 × 128). In addition, mice underwent another session under anesthesia to
408 acquire high resolution T2 image (TR = 6000 ms, TE = 8.8 ms, RARE-factor = 16, FA = 180°, 36 coronal
409 slices, 100 × 100 × 400 μm^3 voxels, FOV 16 × 16 mm^2, matrix size of 160 × 160, 10 averages) and
410 diffusion tensor imaging data (DTI) with a diffusion-weighted spin-echo echo-planar imaging (EPI)
411 pulse sequence (TR = 9000 ms, TE = 21.68 ms, $\Delta/\delta = 11/2.6$ ms, 4 EPI segments, 30 gradient directions
412 with a single b-value at 1000 s/mm^2 and three images with b-value of 0 s/mm^2 (B0), 36 slices, 100 ×
413 100 × 400 μm^3 voxels, FOV 16 × 16 mm^2, matrix size of 160 × 160, 2 averages). Each DTI acquisition
414 took 39.6 min.
415

416 ## 1.3. Data processing

417 **Intrinisc functional connectivity data:**

418 fMRI data preprocessing procedure was validated in a previous study (22). Briefly, the first two time
419 points were removed for T1-equilibration effects, slice-dependent time shifts were compensated,
420 head motion was corrected using rigid body correction, volumes were registered to a downsampled
421 version of the Allen Mouse Brain Atlas, and data underwent intensity normalization. Then, motion
422 scrubbing procedure was applied to remove motion-related artifacts as previously shown. A
423 rigorous censoring criteria were used including frame displacement (FD) of 50 μm and temporal
424 derivative root mean square variance over voxels (DVARS) of 105% of median. An augmented
425 temporal mask of 1 frame before and 2 frames after detected motion was used and sequences of
426 less than 5 included frames were also censored. Runs with less than 50 frames, and sessions with
427 less than 125 frames (5.2 mins) were excluded. The average number of included sessions per mouse
428 was 6.31±0.82 (mean±SD) for the F1 hybrid mice and 3.71±2.21 for the C57BL/6 inbred mice. Total
429 included time per session was 15.7±4.4 (minutes per session, mean±SD) and 11.41±3.67,
430 respectively.
431

432 After motion scrubbing, resting-state fMRI specific preprocessing procedure was applied including
433 demeaning and detrending, nuisance regression of 6 motion axes, ventricular and white matter
434 signals and their derivatives, temporal filter (0.009 < f < 0.08 Hz), and spatial smoothing (Gaussian
435 kernel with FWHM of 450 μm.) The C57BL/6 group was preprocessed both with and without global

signal regression to test the effects of this procedure on structure-function relations.

To estimate functional connectomes, we build a parceled volume with a resolution compatible with the fMRI technical constraints by manipulating the Allen Mouse Brain Connectivity Atlas (18) downloaded through The Virtual Brain (9, 21). The volume was registered to the space of the functional data ('target.nii.gz') using the nearest neighbor interpolation (FLIRT software, (51)). The parcellation was reduced only to the areas where the SNR was higher than 12, and that had a volume greater than 10 voxels (>0.1mm^3). Finally, very anterior and posterior areas, such as the main olfactory bulb and cerebellum, were excluded from the parcellation due to registration problems and susceptibility artifacts associated with the head-post implantation. Once the parcellation volume was built, mean BOLD signals were extracted from the voxels composing each parcel, and correlations were calculated from included frames only (based on motion scrubbing).

Diffusion-MRI data:

We processed diffusion-MRI data using MRtrix3 software (28).

The fiber orientation distribution of each voxel was estimated using the Constrained Spherical Deconvolution (CSD, (52)). To obtain the tract streamlines we integrated the field of orientation probability density using both deterministic (SD_Stream, (28)) and probabilistic (iFOD2, (29)) algorithms; in both cases, the tracts number was set to 100 million. The streamlines were then filtered using the SIFT algorithm (53) which selectively reduces the number of tracts exploiting the fiber orientation density information obtained through the CSD in the previous step. The filtered tracts of the right SSp-bfd obtained with probabilistic and deterministic algorithm, for an illustrative mouse, are shown in Figure 2B and 2C respectively. We defined seed regions using the Allen Mouse Brain Connectivity Atlas (18) obtained through the The Virtual Brain (9, 21); after registering the volume in the individual mouse diffusion space, we reduced the parcellation only to those areas whose volume was greater than 250 voxels (>1.125mm^3).

Using the deterministic and probabilistic streamlines and the node parcellation image, we generated a connectome. The connection strength between each pair of nodes was defined as the streamline count between the two nodes scaled by the inverse of the volumes of the two areas. A radial research was performed to assign each streamline end point to a given node. If no node was found inside a sphere of 1 mm radius, the streamline was not assigned to any node. We excluded all self-connections by setting the diagonal elements of the connectome to zero and normalized all connection strengths between 0 and 1. Then, we repeated this procedure for all mice. An example

468 of personalized connectome obtained with probabilistic and deterministic algorithm is shown in
469 Figure 2B and 2C, respectively.
470
471 **Tracer data:**
472 The recent updates of The Virtual Brain software (9, 21) allows us to manipulate the anterograde
473 tracer experiments performed at the Allen Institute (18) in order to obtain a very precise mouse
474 connectome. Unless otherwise specified, the tracer-based connectome is built averaging
475 experiments performed injecting the tracing compound in the areas in the right hemisphere.
476 One of the main differences between tracer and diffusion-MRI technique is the spatial resolution;
477 in order to discard this factor as a cause of diversity in the reconstructed connectome, the seed
478 areas included in the tracer connectome are the same as the ones included in the diffusion-MRI
479 connectome. As for the diffusion-MRI connectome, the self-connections were excluded and the
480 connection strengths were normalized between 0 and 1. The tracer connectome is shown in Figure
481 2D.
482 To evaluate the impact of introducing connections of the left SSs obtained injecting the tracing
483 compound in the left structure (and not in the right structure as generally done in the building
484 procedure) we built tracer-based connectome using the information of just one experiment per area
485 (Figure S6b). In particular in Figure 5B we evaluate how reconstructing left SSs connections using
486 different experiments (14 injection experiments performed in the right SSs and 1 injection
487 experiment in the left SSs) impact the Predictive Power of the tracer connectome.
488

489 1.4. Surrogate connectomes

490 Connectomes derived with different methodologies (e.g. tracer experiments, deterministic or
491 probabilistic diffusion-MRI tractography) give rise to different simulated resting state dynamics.
492 Since in this study we always use the same large-scale model to simulate the functional brain
493 patterns (reduced Wong Wang model in the bistable configuration, see section simulated
494 dynamics), the observed differences are determined uniquely by the different structural
495 organization used to conceptualize the brain network, i.e. the connectome.
496 In order to test different hypotheses about what could be the connectivity properties that give rise
497 to the observed discrepancies in the simulated dynamics, we built different kinds of surrogate
498 connectomes as described in what follows.
499

Averaged connectome: the role of individual variability

In order to assess the role of individual variability in dMRI data, we built an averaged connectome, both for deterministic and probabilistic tractography. We defined the averaged connectome as a matrix whose entry $\acute{w}_{ij}$, i.e. the connection strength between area *i* and area *j*, is the arithmetic mean of the values of the connection strength w_{ij} of the N individual dMRI connectomes containing both area *i* and area *j*:

$$\acute{w}_{ij} = \frac{1}{N}\sum_{n=1}^{N} {w_{ij}}^{n}$$

(1)

where *n* is the connectome index.

Filtered connectome: the role of long range connections

Comparing the connectomes in Figure 2B-D it is possible to notice that the number of long range connections detected with probabilistic, and more dramatically with deterministic, tractography is drastically lower than the one retrieved with the tracer method. It is well known that the accuracy of fiber reconstruction with diffusion-MRI data decreases with fiber distance; however, it is still unclear how to address this methodological limitation.

In order to quantify the impact of long-range connections presence in the simulated system, we filtered down the tracer connectome by removing all the connection not present in the deterministic diffusion-MRI connectomes. The filtered tracer connectome is shown in Figure 3A.

Symmetrized and asymmetrized connectome: the role of fiber directionality

The incapacity to detect fiber directionality is one of the main drawbacks of dMRI method.

In order to understand the influence of this property in the simulated system, we symmetrized the tracer connectome and we asymmetrized the diffusion-MRI connectome.

Symmetrized tracer connectome:

For each asymmetric matrix exists one, and only one, decomposition that enables us to find the corresponding symmetric matrix: each generic matrix A can be decomposed in its symmetric and asymmetric part as:

$$A = A^{\text{sym}} + A^{\text{asym}} = \underbrace{\frac{1}{2}(A + A^T)}_{\text{symmetric part}} + \underbrace{\frac{1}{2}(A - A^T)}_{\text{asymmetric part}}$$

thus, symmetrizing a matrix means neglecting its asymmetric part.

Following this consideration, the tracer symmetric connectome was defined as the matrix whose entries $\hat{t}_{ij}$ are defined as:

$$\hat{t}_{ij} = \frac{t_{ij} + t_{ji}}{2}$$

(2)

where t_{ij} represents the original tracer connection strength between area *i* and area *j*.

The symmetric tracer structural connectivity is shown in Figure 3A.

<u>Asymmetrized dMRI connectome:</u>

As opposed to symmetrizing a matrix which is a straightforward procedure, a-symmetrizing a matrix is an ill-posed problem, since it means introducing a new degree of freedom in the system, and not a unique solution exists. Thus, to find the asymmetric version of the dMRI connectome we assumed some constraints: we injected in each connection the same degree of asymmetry contained in the respective tracer connection, while preserving the dMRI weight balancing. In other words, our asymmetrization method assumes that the degree of asymmetry is independent on the connection strength value.

We defined the asymmetry degree μ_{ij}between connection *i* and connection *j* as:

$$\mu_{ij} = \begin{cases} \frac{t_{ij}}{t_{ji}}, \wedge\, t_{ij} \leq t_{ji} \\ \frac{t_{ji}}{t_{ij}}, \wedge\, t_{ij} > t_{ji} \end{cases}$$

(3)

so that:

if the *ij* connection is symmetric: $t_{ij} = t_{ji} \Rightarrow \mu_{ij} = +1$

if the *ij* connection is anti-symmetric: $t_{ij} = -t_{ji} \Rightarrow \mu_{ij} = -1$

However, since the connection strengths in the connectome are always positively defined, μ_{ij} is a value always between 0 and 1.

The information on the directionality of the tracer connection between area *i* and area *j*, measured by μ_{ij}, are inserted in the diffusion-MRI connectome by modifying the original connection w_{ij} in

$\check{w}_{ij}$:

$$\mu_{ij} = \frac{t_{ij}}{t_{ji}} = \frac{\check{w}_{ij}}{\check{w}_{ji}}$$

Specifically, we defined $\check{w}_{ij} = w_{ij} - k$ and $\check{w}_{ji} = w_{ji} + k$, where k is defined as:

$$\mu_{ij} = \frac{\check{w}_{ij}}{\check{w}_{ji}} = \frac{w_{ij} - k}{w_{ji} + k} \Rightarrow k = w_{ij}\frac{1 - \mu_{ij}}{1 + \mu_{ij}}$$

(4)

It is important to notice that the asymmetrization of the connectome does not imply the introduction of new connections: if the original diffusion-MRI connection w_{ij} is absent it follows, from the last equation, that also the increment k will be zero.

The asymmetrized deterministic connectome is shown in Figure 3C.

<u>Hybrid connectome: the role of individual connections</u>

We aimed to study the influence of the technique, the dMRI or the tracer one, in reconstructing the connections of a specific brain area. For this purpose, we built surrogate connectomes where all the brain wirings were reconstructed with deterministic dMRI except the connections of the region under examination that were measured with anatomical tracing.

In particular, for each deterministic dMRI connectome *W*, composed of N brain areas, we generated *N* different connectomes W^k by substituting the incoming and outgoing non-zero dMRI connections of area *k* with the corresponding tracer connections. The entry $w_{ij}^k$of the hybrid connectome W^k are defined as:

$$w_{ij}^k = \begin{cases} w_{ij} \text{if } i, j \in [1,2, \dots, k+1, k-1, \dots, N] \\ t_{kj} \text{ if } i = k \text{and } w_{ij} \neq 0 \\ t_{ik} \text{ if } j = k \text{and } w_{ij} \neq 0 \end{cases}$$

where w_{ij} and t_{ij} represent the connection strength of the original-individual deterministic dMRI and the original tracer connectome, respectively.

It is important to notice that this operation does not imply the introduction of new connections.

<u>1.5.</u> Comparing anatomical connectivities

We quantify the difference in the connectomes using both statistical tools (the Mann-Whitney test

and the Pearson correlation) and graph theory tools (54).

U-static as a measure of connectome similarity

We used the Mann-Whitney test to check if the connections strength of connectomes W_i and W_j come from the same distribution. The null hypothesis of the test, H_0, is that the probability of an observation, i.e. a connection strength, of the connectome W_i exceeding an observation from population W_j equals the probability of an observation W_j exceeding an observation from sample W_i:

$$H_0: P(W_i > W_j) = P(W_i < W_j)$$

the alternative hypothesis, H_1, is:

$$H_1: P(W_i > W_j) \neq P(W_i < W_j)$$

The test involves the calculation of a statistic, usually called U.

For sample size above 20, which is our case, the distribution of the U variable under the null hypothesis can be approximated using the normal distribution. The U variable ranges between 0 and $n_1 n_2$, where n_1 and n_2 are the dimensionalities of the two connectomes. For $U \leq U^* = n_1 n_2/2$ the test states that the H_0 can be rejected.

It follows that it is possible to normalize the U value between 0 and 1, by dividing it by the product of the dimensionality of the two connectomes; in this case the discriminator value U^* is 0.5.

Graph theory measures

We characterized anatomical mouse brain structures using graph theory tools; in particular, we characterized each connectome by calculating its degree distribution and its topological properties.

Degree distribution

For each connectome, we calculated the directed degree distribution as:

$$k_i = k_i^{\text{out}} + k_i^{\text{in}} = \sum_j w_{ij} + \sum_i w_{ij}$$

We quantified the probability that the degree distribution comes from a given theoretical distribution through the Kolmogorov Smirnov test.

Topological structure

Topological measures as clustering coefficient and shortest path (and consequently the small world

index) are strictly dependent on graph densities, and thus the comparison of topological measures of different graphs should be carefully accomplished (55).

To avoid spurious results from the comparison, we used a modified version of the small world index, i.e. the Small World Propensity (SWP), as introduced by (36).

Pearson correlation as a measure of area's connections peculiarity:

We quantified the peculiarity of an area's connections of a certain animal *m* by calculating the averaged Pearson correlation between the area's connections of the animal *m* and the area's connections in the other animals.

Euclidean distance as quantification of hemispheric functional lateralization:

We quantified the functional lateralization of a given region *x* as the Euclidean distance between the functional connections of the left area *x* and the functional connections of the right area *x*.

1.6. Simulated resting state dynamics

Using the previously described connectomes we conceptualized the mouse brain as a neuronal network. The mean activity of each brain region, i.e. the network's node, was defined by the reduced Wong Wang model (23). In this approach, the dynamics of a region is given by the whole dynamics of excitatory and inhibitory populations of leaky integrate-and-fire neurons interconnected via NMDA synapses. Here we take into account the model with a further reduction performed in (13): the dynamics of the output synaptic NMDA gating variable S of the *i*-th brain area is strictly bound to the collective firing rate H_i. The resulting model is given by the following coupled equations:

$$\frac{dS_i}{dt} = \frac{-S_i}{\tau_s} + (1 - S_i)\gamma H_i + \sigma\eta_i(t) \tag{5}$$

$$H_i = \frac{ax_i - b}{1 - exp\big(-d(ax_i - b)\big)} \tag{6}$$

$$x_i = \omega J_N S_i + J_N G \sum_j w_{ij} S_j + I_o \tag{7}$$

where x_i is the synaptic input to the *i*-th region. γ is a kinetic parameter fixed to 0.641, τ_s is the

645 NMDA decay time constant and its value is 100 ms; a, b and d are the parameters of the input and
646 output function H and are respectively equal to 270 nC^{-1}, 108 Hz, 0.154 s. $J_N = 0.2609nA$ is an
647 intensity scale for the synaptic input current. ω is the local excitatory recurrence and I_o is the
648 external input current. G is the coupling strength i.e. a scalar parameter which scales all the
649 connection strengths w_{ij} without altering the global topology of the network. We set the noise
650 amplitude σ of the normally distributed stochastic variable η_i to 0.015 since this level of noise is
651 able to sustain brain states oscillations.
652 The local excitatory recurrence, ω, and of the local excitatory recurrence and I_o are set to 0.3 nA
653 and 1, respectively, in order to enrich the non-linearity of the dynamics of each brain region. In this
654 case, studying the dynamics of isolated brain areas ($G = 0$ in equation (7), it is possible to notice
655 that each brain area is in a bistable state and it oscillates between high and low activity fixed points
656 (14). It has been noticed in (14) that enriching the non-linearity of each brain areas introduces global
657 network's attractors that are not in trivial relation with the anatomical connectivity; this model
658 offers the chance to reproduce the non-stationary features of the functional connectivity patterns,
659 as shown by the checkboard pattern of the simulated FCD in Figure S1b.
660 For each connectome, we identified the coupling strength values for which the system is
661 experiencing multistability. The optimal coupling strength range is defined as the values for which
662 the system low and high states coexist, and it is identified by building the system's bifurcation
663 diagram as described in (13).
664 The brain activity, for each connectome, is simulated for 40 values of coupling strength that equally
665 span between 0 and M, where M corresponds to the coupling strength value for which the low state
666 (identified with the previous method), disappears. The simulations obtained from each
667 connectome, for different coupling strength value, are used to calculate the predictive power of the
668 connectome as explained in the section.
669
670 **Integration scheme and BOLD signals**
671 Model equations are numerically solved using the Euler Maruyama integration method with a fixed
672 integration step of 0.1 ms. Simulated BOLD signal is obtained by converting the simulated synaptic
673 activity (equation (5) using the Balloon-Windkessel method (56) with the default value
674 implemented in The Virtual Brain (57).
675 The BOLD time-series are down-sampled to 2.5 sec according to the temporal resolution of the
676 experimental data.

1.7. Resting state signals analysis

Functional connections in the experimental and simulated time-series are explored from both spatial and temporal point of views using the Functional Connectivity (FC) and the Functional Connectivity Dynamics (FCD), respectively. We also explored the relation between functional links by estimating the Functional Meta-Connectivity (FMC).

Functional Connectivity (FC)

The FC matrix is defined as the matrix whose *ij*-th element is the Pearson correlation between the BOLD signal of the brain region *i* and of the brain region *j*. An example of empirical and simulated FC is shown in figure 1.

Functional Connectivity Dynamics (FCD)

The FCD matrix for the experimental and simulated signals is calculated using the sliding windows approach (14, 24).

To estimate the FCD, the entire BOLD time-series is divided in time windows of a fixed length (2 min) and with a spanning of 2.5 sec; the data points within each window centered at the time $t_i$were used to calculate FC(t_i).

The *ij*-th element of the FCD matrix is calculated as the Pearson correlation between the upper triangular part of the FC(t_i) matrix arranged as a vector and the upper triangular part of the FC(t_j) matrix arranged as a vector.

In order to observe signal correlations at frequency greater than the typical one of the BOLD signals, the sliding window length is fixed to 2 min, since, as demonstrated by (Leonardi and Van De Ville 2015), the non-spurious correlations in the FCD are limited by high-pass filtering of the signals with a cut-off equal to the inverse of the window length.

An example of empirical and simulated FCD is shown in Figure 1.

The typical FCD matrix during resting-state has a checkboard appearance (see experimental FCD in Figure 1) indicating that the system is switching between stable networks configuration (14, 24). We quantified the *switching degree* of the simulated and experimental system as the variance of the triangular part of the FCD once excluded the overlapping entries (i.e. the entries of the FCD matrix that quantify the correlation of FCs calculated over the sliding window of overlapping time interval). We called this quantity clue of switching (cs).

Functional Meta-Connectivity (FMC)

To compare the dynamical evolution of the functional connections between different systems we calculate, for each system, the FMC. The FMC, of a BOLD signals of *N* areas, is a $N^2 \mathrm{x} N^2$ matrix that quantifies the inter-region functional correlation of the system. The *ij*-th element of the FMC represents the Pearson correlation between the temporal evolution of the *i*-th functional link and the *j*-th functional link.

1.8. Comparing experimental and simulated BOLD signals

We quantified the ability of a given connectome to be used as a skeleton of the virtual system by comparing the accordance between the simulated functional connections, generated using that connectome, and the functional connections arranged during the experimental resting state recordings.

As discussed in the article we used the FC as the metric for quantifying the experimental and simulated functional connections. Indeed, although the FC metric is not able to capture the non-stationary nature of the resting state signals, the static functional connections are stable across resting state recordings in the same animal; on the other hand, FMC, that is able to quantify the dynamical evolution of the functional connections, is not stable across resting state recordings (see Figure S1), and thus cannot be used for quantifying the goodness of the simulated activity.

The simulated functional network is generally composed of more areas than the experimental one since the simulation is based on the anatomical information that has a greater spatial resolution than the functional ones. Thus, in order to correlate the eFC and the sFC we reduced them to the same number of areas. For each virtual mouse brain we simulated for different values of the coupling strength G and then select the value of G for which the simulated neuronal network is able to obtain the more realistic outcome, i.e. the maximum correlation between the empirical and simulated FC (12, 14, 58).

For each mouse, *m*, and each session, *d*, we defined the PP of a given connectome c as the maximum Pearson correlation between empirical the FC (eFC) and the simulated FC (sFC) obtained for the different coupling strength values G:

$$PP(c,m,d) = \max_{G}\{corr[sFC(c,G), eFC(m,d)]\}$$

The PP of a given connectome $PP(c)$ is the mean over all the mice and the sessions of the $PP(c, m, d)$:

$$PP(c) = \underset{m,d}{mean}\{PP(c, m, d)\}$$

Since the tracer connectomes and the diffusion-MRI averaged connectomes are not derived from a specific animal, the corresponding simulated-FCs are correlated with all the functional data composing our dataset (irrespective to the mouse in which the functional data were recorded). Diffusion-MRI connectomes, instead, are specific of each animal, and thus the FCs derived from the connectome of a certain mouse are correlated only with the empirical FC recorded in the same animal.

In order to assess the significance of the difference in PP of differently derived connectomes we used the p-value calculated through the Welch's test.

REFERENCES:

1. Sporns O, Tononi G, Kötter R (2005) The human connectome: a structural description of the human brain. *PLoS Comput Biol* 1(4):e42.

2. Yeh F-C, et al. (2016) Quantifying differences and similarities in whole-brain white matter architecture using local connectome fingerprints. *PLoS Comput Biol* 12(11):e1005203.

3. Mikhael SS, et al. (2019) Manually-parcellated gyral data accounting for all known anatomical variability. *Sci Data* 6:190001.

4. Biswal B, Zerrin Yetkin F, Haughton VM, Hyde JS (1995) Functional connectivity in the motor cortex of resting human brain using echo-planar mri. *Magn Reson Med* 34(4):537–541.

5. Finn ES, et al. (2015) Functional connectome fingerprinting: identifying individuals using patterns of brain connectivity. *Nat Neurosci* 18(11):1664–1671.

6. Gratton C, et al. (2018) Functional brain networks are dominated by stable group and individual factors, not cognitive or daily variation. *Neuron* 98(2):439–452.

7. Mueller S, et al. (2013) Individual variability in functional connectivity architecture of the human brain. *Neuron* 77(3):586–595.

8. Finn ES, Todd Constable R (2016) Individual variation in functional brain connectivity: implications for personalized approaches to psychiatric disease. *Dialogues Clin Neurosci* 18(3):277–287.

9. Sanz Leon P, et al. (2013) The Virtual Brain: a simulator of primate brain network dynamics. *Front Neuroinformatics* 7:10.

10. Ghosh A, Rho Y, McIntosh AR, Kötter R, Jirsa VK (2008) Noise during rest enables the exploration of the brain's dynamic repertoire. *PLoS Comput Biol* 4(10):e1000196.

11. Jirsa VK, Jantzen KJ, Fuchs A, Kelso JAS (2002) Spatiotemporal forward solution of the EEG and MEG using network modeling. *IEEE Trans Med Imaging* 21(5):493–504.

12. Deco G, Jirsa VK, McIntosh AR (2011) Emerging concepts for the dynamical organization of resting-state activity in the brain. *Nat Rev Neurosci* 12(1):43.

13. Deco G, et al. (2013) Resting-state functional connectivity emerges from structurally and dynamically shaped slow linear fluctuations. *J Neurosci* 33(27):11239–11252.

14. Hansen EC, Battaglia D, Spiegler A, Deco G, Jirsa VK (2015) Functional connectivity dynamics: modeling the switching behavior of the resting state. *Neuroimage* 105:525–535.

15. Jirsa VK, et al. (2017) The Virtual Epileptic Patient: Individualized whole-brain models of epilepsy spread. *NeuroImage* 145:377–388.

16. Wedeen VJ, et al. (2008) Diffusion spectrum magnetic resonance imaging (DSI) tractography of crossing fibers. *Neuroimage* 41(4):1267–1277.

17. Kötter R (2007) Anatomical Concepts of Brain Connectivity. *Handbook of Brain Connectivity*,

Understanding Complex Systems. (Springer, Berlin, Heidelberg), pp 149–167.

18. Oh SW, et al. (2014) A mesoscale connectome of the mouse brain. *Nature* 508(7495):207.

19. Gămănuţ R, et al. (2018) The Mouse Cortical Connectome, Characterized by an Ultra-Dense Cortical Graph, Maintains Specificity by Distinct Connectivity Profiles. *Neuron* 97(3):698-715.e10.

20. Ypma RJ, Bullmore ET (2016) Statistical analysis of tract-tracing experiments demonstrates a dense, complex cortical network in the mouse. *PLoS Comput Biol* 12(9):e1005104.

21. Melozzi F, Woodman MM, Jirsa VK, Bernard C (2017) The Virtual Mouse Brain: A Computational Neuroinformatics Platform To Study Whole Mouse Brain Dynamics. *eNeuro*:ENEURO–0111.

22. Bergmann E, Zur G, Bershadsky G, Kahn I (2016) The organization of mouse and human cortico-hippocampal networks estimated by intrinsic functional connectivity. *Cereb Cortex*:1–16.

23. Wong K-F, Wang X-J (2006) A recurrent network mechanism of time integration in perceptual decisions. *J Neurosci* 26(4):1314–1328.

24. Allen EA, et al. (2014) Tracking whole-brain connectivity dynamics in the resting state. *Cereb Cortex* 24(3):663–676.

25. Grandjean J, et al. (2017) Dynamic reorganization of intrinsic functional networks in the mouse brain. *NeuroImage* 152:497–508.

26. Laumann TO, et al. (2015) Functional system and areal organization of a highly sampled individual human brain. *Neuron* 87(3):657–670.

27. Van Dijk KRA, et al. (2009) Intrinsic Functional Connectivity As a Tool For Human Connectomics: Theory, Properties, and Optimization. *J Neurophysiol* 103(1):297–321.

28. Tournier J-D, Calamante F, Connelly A (2012) MRtrix: diffusion tractography in crossing fiber regions. *Int J Imaging Syst Technol* 22(1):53–66.

29. Tournier JD, Calamante F, Connelly A (2010) Improved probabilistic streamlines tractography by 2nd order integration over fibre orientation distributions. *Proceedings of the International Society for Magnetic Resonance in Medicine*, p 1670.

30. Zalesky A, et al. (2016) Connectome sensitivity or specificity: which is more important? *Neuroimage* 142:407–420.

31. Fox MD, Zhang D, Snyder AZ, Raichle ME (2009) The global signal and observed anticorrelated resting state brain networks. *J Neurophysiol* 101(6):3270–3283.

32. Craddock RC, et al. (2013) Imaging human connectomes at the macroscale. *Nat Methods* 10(6):524–539.

33. Li L, Rilling JK, Preuss TM, Glasser MF, Hu X (2012) The effects of connection reconstruction method on the interregional connectivity of brain networks via diffusion tractography. *Hum Brain Mapp* 33(8):1894–1913.

34. Kale P, Zalesky A, Gollo LL (2018) Estimating the impact of structural directionality: How reliable are undirected connectomes? *Netw Neurosci* 2(02):259–284.

35. Watts DJ, Strogatz SH (1998) Collective dynamics of ‘small-world’networks. *nature* 393(6684):440.

36. Muldoon SF, Bridgeford EW, Bassett DS (2016) Small-World Propensity and Weighted Brain Networks. *Sci Rep* 6(1). doi:10.1038/srep22057.

37. Mohajerani MH, et al. (2013) Spontaneous cortical activity alternates between motifs defined by regional axonal projections. *Nat Neurosci* 16(10):1426.

38. Stafford JM, et al. (2014) Large-scale topology and the default mode network in the mouse connectome. *Proc Natl Acad Sci* 111(52):18745–18750.

39. Díaz-Parra A, Osborn Z, Canals S, Moratal D, Sporns O (2017) Structural and functional, empirical and modeled connectivity in the cerebral cortex of the rat. *Neuroimage* 159:170–184.

40. Zimmermann J, Griffiths J, Schirner M, Ritter P, McIntosh AR (2018) Subject specificity of the correlation between large-scale structural and functional connectivity. *Netw Neurosci* 3(1):90–106.

41. Rangaprakash D, Wu G-R, Marinazzo D, Hu X, Deshpande G (2018) Hemodynamic response function (HRF) variability confounds resting-state fMRI functional connectivity. *Magn Reson Med* 80(4):1697–1713.

42. Desai M, et al. (2010) Mapping brain networks in awake mice using combined optical neural control and fMRI. *J Neurophysiol* 105(3):1393–1405.

43. Schlegel F, Schroeter A, Rudin M (2015) The hemodynamic response to somatosensory stimulation in mice depends on the anesthetic used: implications on analysis of mouse fMRI data. *Neuroimage* 116:40–49.

44. Silva AJ, et al. (1997) Mutant mice and neuroscience: recommendations concerning genetic background. *Neuron* 19(4):755–759.

45. Sittig LJ, et al. (2016) Genetic background limits generalizability of genotype-phenotype relationships. *Neuron* 91(6):1253–1259.

46. Shinohara Y, Hosoya A, Hirase H (2013) Experience enhances gamma oscillations and interhemispheric asymmetry in the hippocampus. *Nat Commun* 4:1652.

47. Fornito A, Zalesky A, Breakspear M (2015) The connectomics of brain disorders. *Nat Rev Neurosci* 16(3):159.

48. Calhoun VD, Lawrie SM, Mourao-Miranda J, Stephan KE (2017) Prediction of Individual Differences from Neuroimaging Data. *NeuroImage* 145:135–136.

49. Deco G, Kringelbach ML (2014) Great Expectations: Using Whole-Brain Computational Connectomics for Understanding Neuropsychiatric Disorders. *Neuron* 84(5):892–905.

50. Besson P, et al. (2017) Anatomic consistencies across epilepsies: a stereotactic-EEG informed high-resolution structural connectivity study. *Brain* 140(10):2639–2652.

51. Greve DN, Fischl B (2009) Accurate and robust brain image alignment using boundary-based registration. *Neuroimage* 48(1):63–72.

52. Tournier J-D, Calamante F, Connelly A (2007) Robust determination of the fibre orientation distribution in diffusion MRI: non-negativity constrained super-resolved spherical deconvolution. *Neuroimage* 35(4):1459–1472.

53. Smith RE, Tournier J-D, Calamante F, Connelly A (2013) SIFT: spherical-deconvolution informed filtering of tractograms. *Neuroimage* 67:298–312.

54. Rubinov M, Sporns O (2010) Complex network measures of brain connectivity: uses and interpretations. *Neuroimage* 52(3):1059–1069.

55. Ginestet CE, Nichols TE, Bullmore ET, Simmons A (2011) Brain network analysis: separating cost from topology using cost-integration. *PloS One* 6(7):e21570.

56. Friston KJ, Mechelli A, Turner R, Price CJ (2000) Nonlinear responses in fMRI: the Balloon model, Volterra kernels, and other hemodynamics. *NeuroImage* 12(4):466–477.

57. Sanz-Leon P, Knock SA, Spiegler A, Jirsa VK (2015) Mathematical framework for large-scale brain network modeling in The Virtual Brain. *Neuroimage* 111:385–430.

58. Deco G, Jirsa VK, McIntosh AR (2013) Resting brains never rest: computational insights into potential cognitive architectures. *Trends Neurosci* 36(5):268–274.

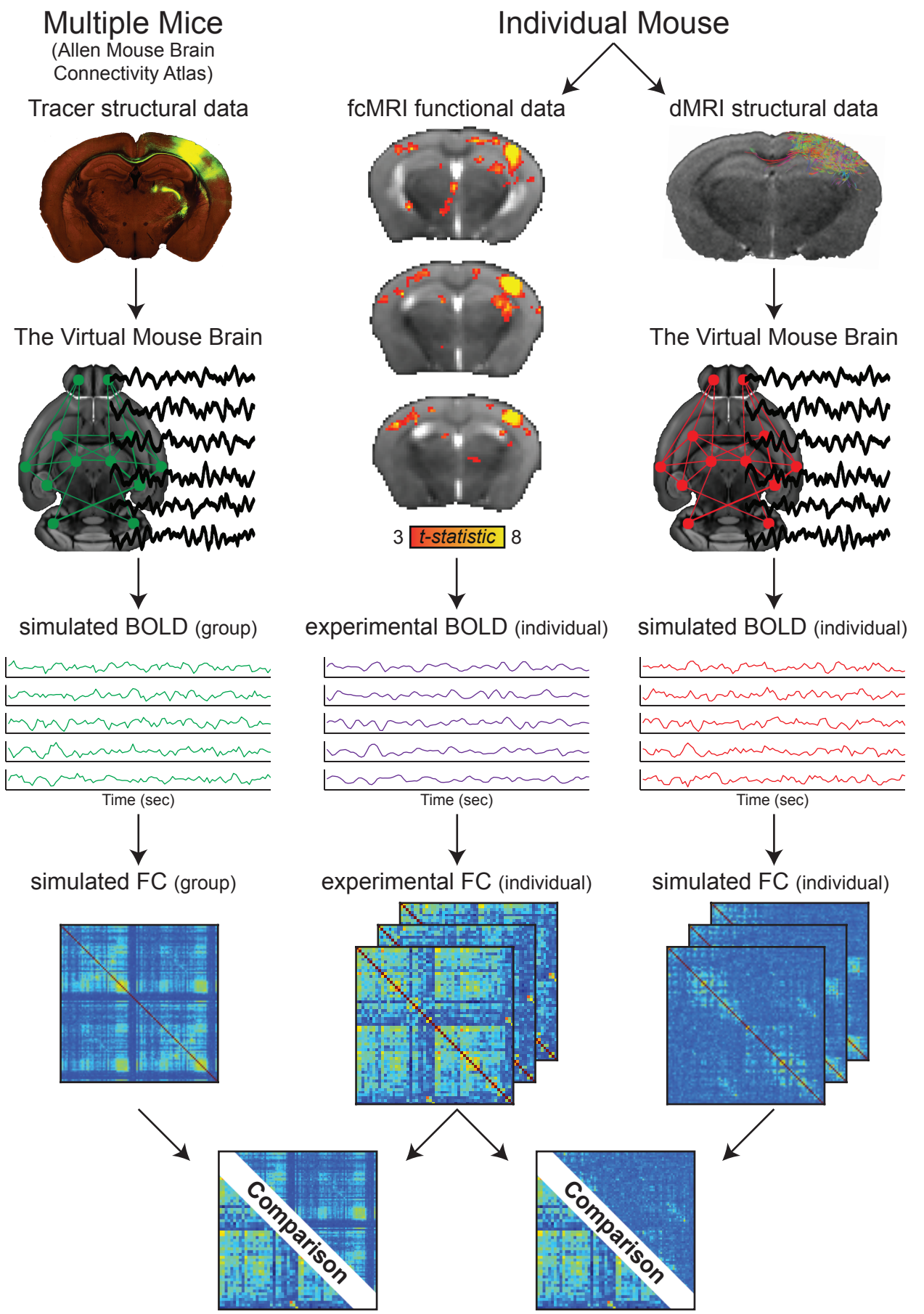
Multiple Mice
(Allen Mouse Brain Connectivity Atlas)
Individual Mouse
Tracer structural data
fcMRI functional data
dMRI structural data
The Virtual Mouse Brain
The Virtual Mouse Brain
3
t-statistic
8
simulated BOLD (group)
experimental BOLD (individual)
simulated BOLD (individual)
Time (sec)
Time (sec)
Time (sec)
simulated FC (group)
experimental FC (individual)
simulated FC (individual)
Comparison
Comparison

Figure 1

Experimental workflow. Each mouse is scanned to obtain both SC and FC data. The virtual mouse brain uses dMRI-based SC to generate *in-silico* BOLD activity. The simulated and experimental brain dynamics are compared through a static-FC metric to estimate the predictive power. Then, the results are compared to the predictive power of the gold standard Allen SC. To illustrate structure-function relations at the level of the individual mouse, we defined a region of interest in the barrel-related primary somatosensory cortex (SSp-bfd) and extracted a dMRI-based tractography and a t-statistic map (calculated from 7 recording sessions of the same mouse, $p < 0.01$, uncorrected, voxel extent = 20).

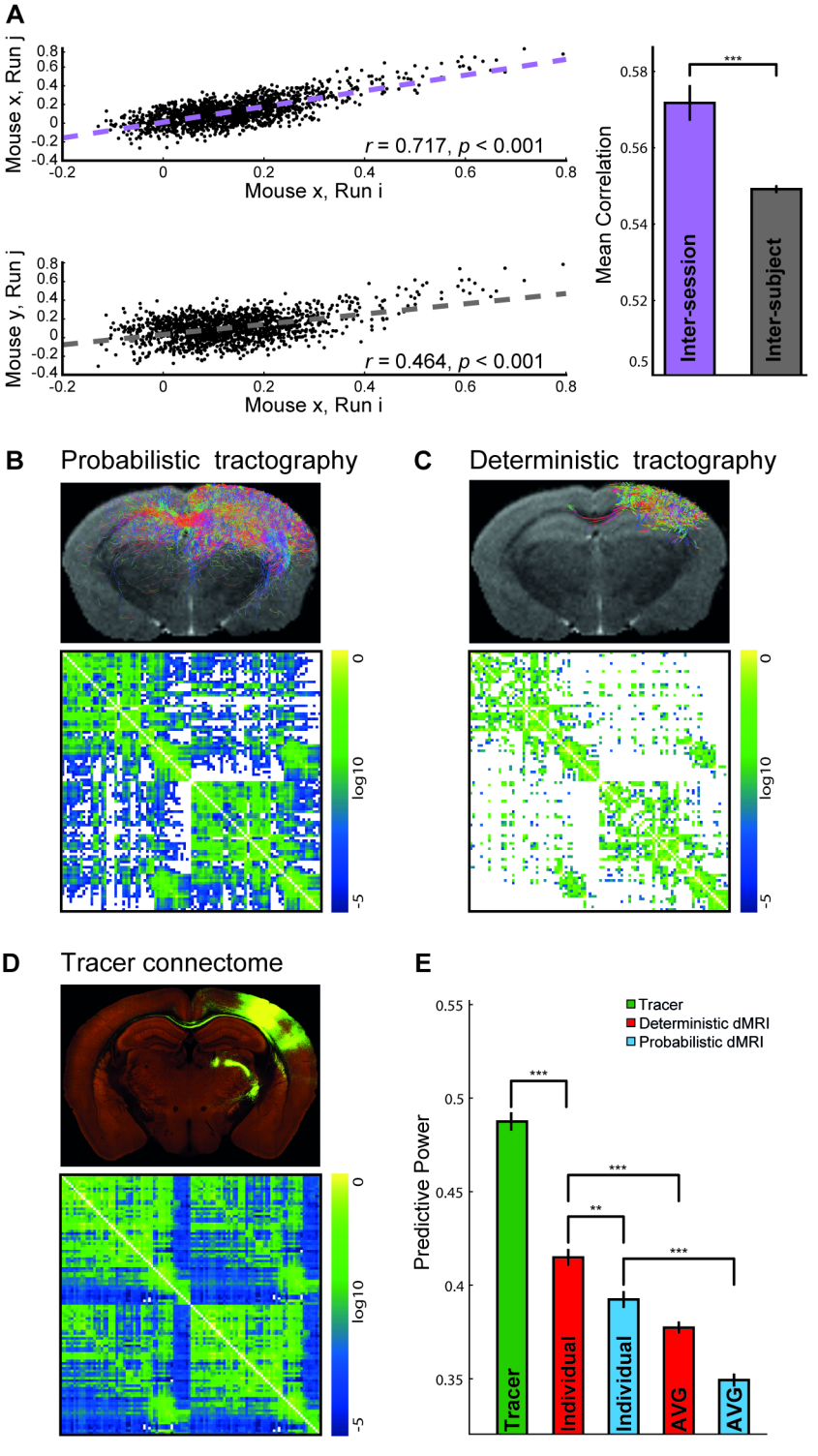
A
Mouse x, Run j
Mouse x, Run i
r = 0.717, p < 0.001
Mouse y, Run j
Mouse x, Run i
r = 0.464, p < 0.001
Mean Correlation
***
Inter-session
Inter-subject
B
Probabilistic tractography
log10
C
Deterministic tractography
log10
D
Tracer connectome
log10
E
Tracer
Deterministic dMRI
Probabilistic dMRI
Predictive Power
***
***
**
***
Tracer
Individual
Individual
AVG
AVG

Figure 2

(A) FC reliability was evaluated by comparing functional connectivity estimates between sessions. Representative scatter plots (*left*) show the correlations between sessions of the same mouse (*inter-session, top*) or between sessions of different mice (inter-subject, *bottom*). Quantification of inter-session and inter-subject similarities in the whole dataset (right) revealed that inter-session similarity is significantly higher than inter-subject similarity. Welch's test ***P<0.001. (B) Probabilistic and (C) deterministic connections for the right barrel-related primary somatosensory cortex (SSp-bfd, *top*) and for the whole brain (*bottom*) of an individual mouse. (D) Tracer-based connections from SSp-bfd (*top*) and group tracer-based SC matrix (the Allen SC*, bottom*). (E) Predictive power of simulations using different types of tracer- and dMRI-based SCs. dMRI-based simulations were performed using individual or group-averaged dMRI (AVG). Welch's test **P<0.01 ***P<0.001.

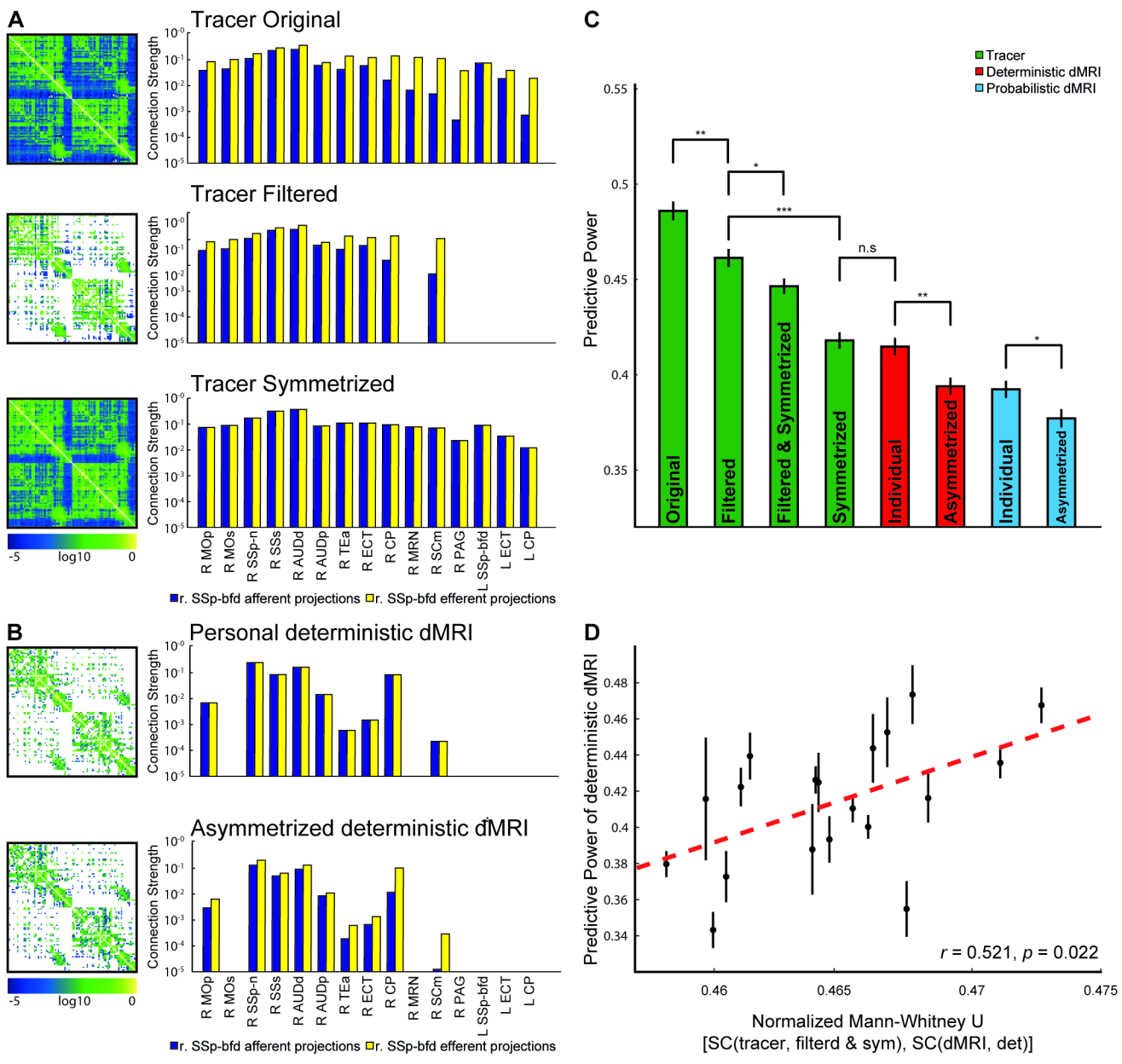
A
Tracer Original
Tracer Filtered
Tracer Symmetrized
Connection Strength
-5
log10
0
R MOp
R MOs
R SSp-n
R SSs
R AUDd
R AUDp
R TEa
R ECT
R CP
R MRN
R SCm
R PAG
L SSp-bfd
L ECT
L CP
r. SSp-bfd afferent projections
r. SSp-bfd efferent projections
B
Personal deterministic dMRI
Asymmetrized deterministic dMRI
C
Tracer
Deterministic dMRI
Probabilistic dMRI
Predictive Power
Original
Filtered
Filtered & Symmetrized
Symmetrized
Individual
Asymmetrized
Individual
Asymmetrized
n.s
D
Predictive Power of deterministic dMRI
r = 0.521, p = 0.022
Normalized Mann-Whitney U
[SC(tracer, filterd & sym), SC(dMRI, det)]

Figure 3

(A) SC surrogates generated from the tracer-based SC (*left*) and representative connections of the SSp-bfd (*right*). The original, filtered and symmetrized SCs are shown in the top, middle and bottom rows, respectively. (B) A representative individual deterministic-dMRI SC (*left*) and SSp-bfd's connections (*right*) before (*top*) and after (*bottom*) a-symmetrization. (C) Comparison between the performances of different surrogate SC demonstrates the effects of filtering and/or symmetrization of the Allen SC and a-symmetrization of the individual deterministic and probabilistic dMRI-based SCs. Welch's test *P<0.05, **P<0.01, ***p<0.001. (D) The relations between PP of filtered and symmetrized tracer SC and individual deterministic dMRI SCs are quantified through the normalized Mann-Whitney U-static and demonstrate significant correlation. The greater U-values represent greater similarity between individual deterministic dMRI SCs and the Allen SC.

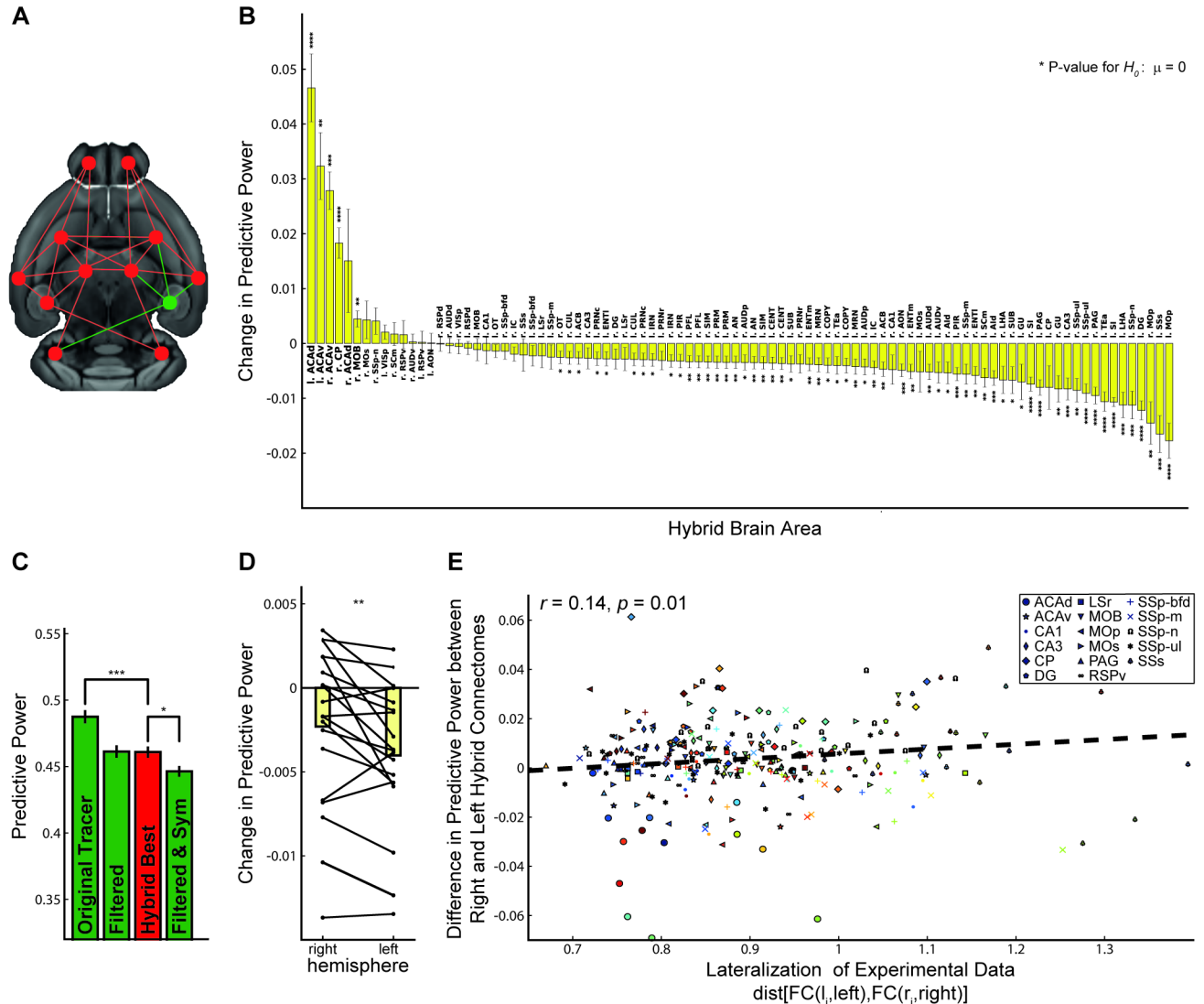
A
B
* P-value for H_o: μ = 0
Change in Predictive Power
Hybrid Brain Area
C
Predictive Power
Original Tracer
Filtered
Hybrid Best
Filtered & Sym
D
Change in Predictive Power
right
left
hemisphere
E
r = 0.14, p = 0.01
Difference in Predictive Power between Right and Left Hybrid Connectomes
Lateralization of Experimental Data
dist[FC(l_i,left),FC(r_i,right)]
ACAd
ACAv
CA1
CA3
CP
DG
LSr
MOB
MOp
MOs
PAG
RSPv
SSp-bfd
SSp-m
SSp-n
SSp-ul
SSs

Figure 4

(A) An illustration of a hybrid SC. The connections between all areas are extracted from dMRI data (*red* nodes and links) except for the connections of a single area, which are obtained from the Allen SC (*green*).

(B) The graph shows the difference in PP between hybrid and individual deterministic dMRI SCs. The change in PP is calculated as the difference between the PP of the hybrid SC and the individual dMRI SC averaged across all sessions and animals. P-values refer to the t-test for the null hypothesis that substituting the tracer connections of a given brain region in the dMRI connectome does not change the PP of the connectome. Nomenclature and abbreviations are listed in Table S1.

(C) A Comparison between the PP of tracer-based and hybrid SCs revealed that connectomes (Hybrid Best), which were generated by replacing the connection of a single area in each mouse, predict experimental FC better than the filtered and symmetrized connectomes (Filtered & Sym). Welch's test: ***P<0.001, *P<0.05.

(D) Comparison between the change in PP following hybridization of left and right brain areas reveals that replacement of left areas' connections decreased the PP more than right areas' connections (paired t-test).

(E) The Differences in PP between right and left hybrid SCs were correlated with the lateralization of experimental FC, which was quantified as the Euclidean distance between left and right functional connections. The closer the lateralization index is to 1, the more similar are the intra-hemispheric left and right area's connections. Different colors label different mice.

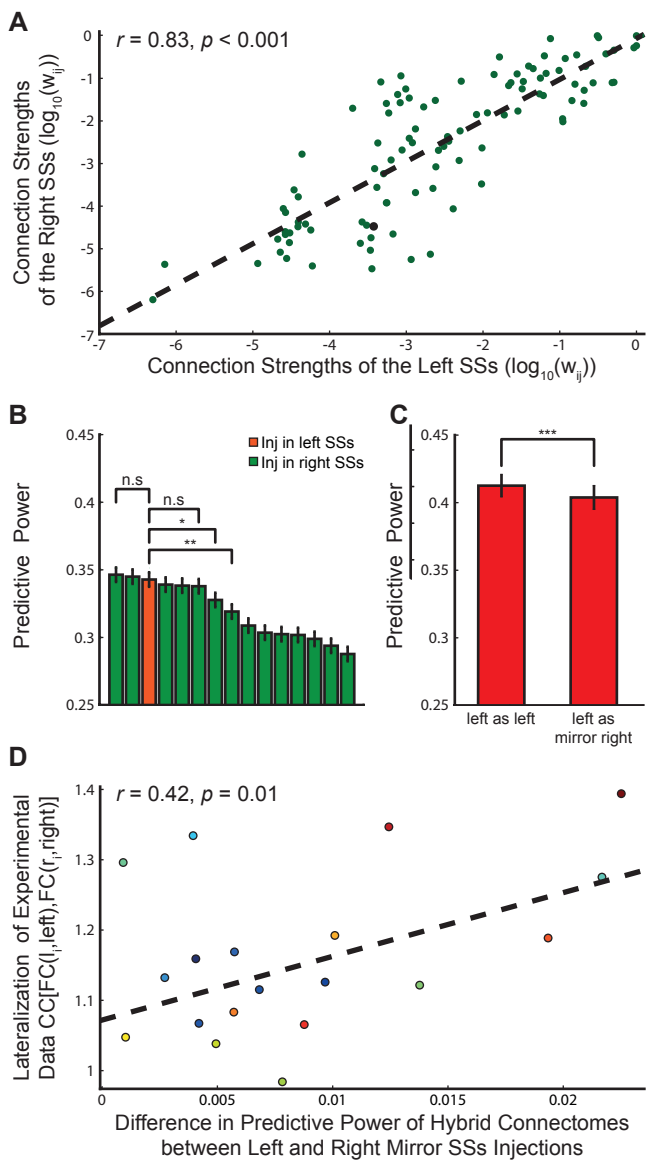
A
r = 0.83, p < 0.001
Connection Strengths of the Right SSs (log10(wij))
Connection Strengths of the Left SSs (log10(wij))
B
Inj in left SSs
Inj in right SSs
n.s
n.s
*
**
Predictive Power
C
***
Predictive Power
left as left
left as mirror right
D
r = 0.42, p = 0.01
Lateralization of Experimental Data CC[FC(li,left),FC(ri,right)]
Difference in Predictive Power of Hybrid Connectomes between Left and Right Mirror SSs Injections

Figure 5:

(A) Relation between fiber projections of the left and right SSs.

(B) The height of the bars represents the predictive power of tracer-based connectomes built using just one injection experiment per area. This procedure differs from the general tracer building procedure used in this work since generally the connections of each region are calculated as the average of the results of all injection experiments performed in that region. The height of the orange bar is the predictive power of the tracer-based connectome whose left SSs connection are reconstructed from the tracer injection experiment in the left SSs. The green bars are the predictive power of the tracer-based connectomes whose left SSs connections are built as the mirror image of the connections measured from each of the 14 experiments performed in the right SSs area.

The statistical difference between the bars is assessed through the Welch's test: *P<0.05, **P<0.01 .

(C) Comparison between the predictive power of hybrid connectomes built as a dMRI-based connectome with left SSs tracer connections reconstructed from the tracer injection experiment in the left SSs or as the mirror image of right tracer connections retrieved from the right SSs experiment whose injection coordinated are closer to those of the left SSs injection experiment.

(D) The Differences in PP between true left and mirror right SSs hybrid SCs are correlated with the lateralization of experimental FC.

Supplementary information

Table S1: List of the acronyms for the different brain regions considered in this work.

Acronym	**Complete name**
ACB	Nucleus accumbens
ACAd	Anterior cingulate area, dorsal part
ACAv	Anterior cingulate area, ventral part
AId	Agranular insular area, dorsal part
AN	Ansiform lobule
AON	Anterior olfactory nucleus
AUDd	Dorsal auditory
AUDp	Primary auditory area
AUDv	Ventral auditory area
CA1	Field CA1
CA3	Field CA3
CENT	Central lobule
COPY	Copula pyramidis
CP	Caudoputamen
CUL	Culmen
DG	Dentate gyrus
ECT	Ectorhinal area
ENTl	Entorhinal area, lateral part
ENTm	Entorhinal area, medial part, dorsal zone
GRN	Gigantocellular reticular nucleus
GU	Gustatory areas
IC	Inferior colliculus
IRN	Intermediate reticular nucleus
LHA	Lateral hypothalamic area
LSr	Lateral septal nucleus, rostral (rostroventral) part
MOB	Main olfactory bulb
MOp	Primary motor area
MOs	Secondary motor area
MRN	Midbrain reticular nucleus
OT	Olfactory tubercle

PAG	Periaqueductal gray
PERI	Perirhinal area
PFL	Paraflocculus
PIR	Piriform area
PRM	Paramedian lobule
PRNc	Pontine reticular nucleus, caudal part
PRNr	Pontine reticular nucleus
RSPd	Retrosplenial area, dorsal part
RSPv	Retrosplenial area, ventral part
SCm	Superior colliculus, motor related
SCs	Superior colliculus, sensory related
SI	Substantia innominata
SIM	Simple lobule
SSp-bfd	Primary somatosensory area, barrel field
SSp-m	Primary somatosensory area, mouth
SSp-n	Primary somatosensory area, nose
SSp-ul	Primary somatosensory area, upper limb
SSs	Supplemental somatosensory area
SUB	Subiculum
TEa	Temporal association areas
UVU	Uvula (IX)
VISp	Primary visual area

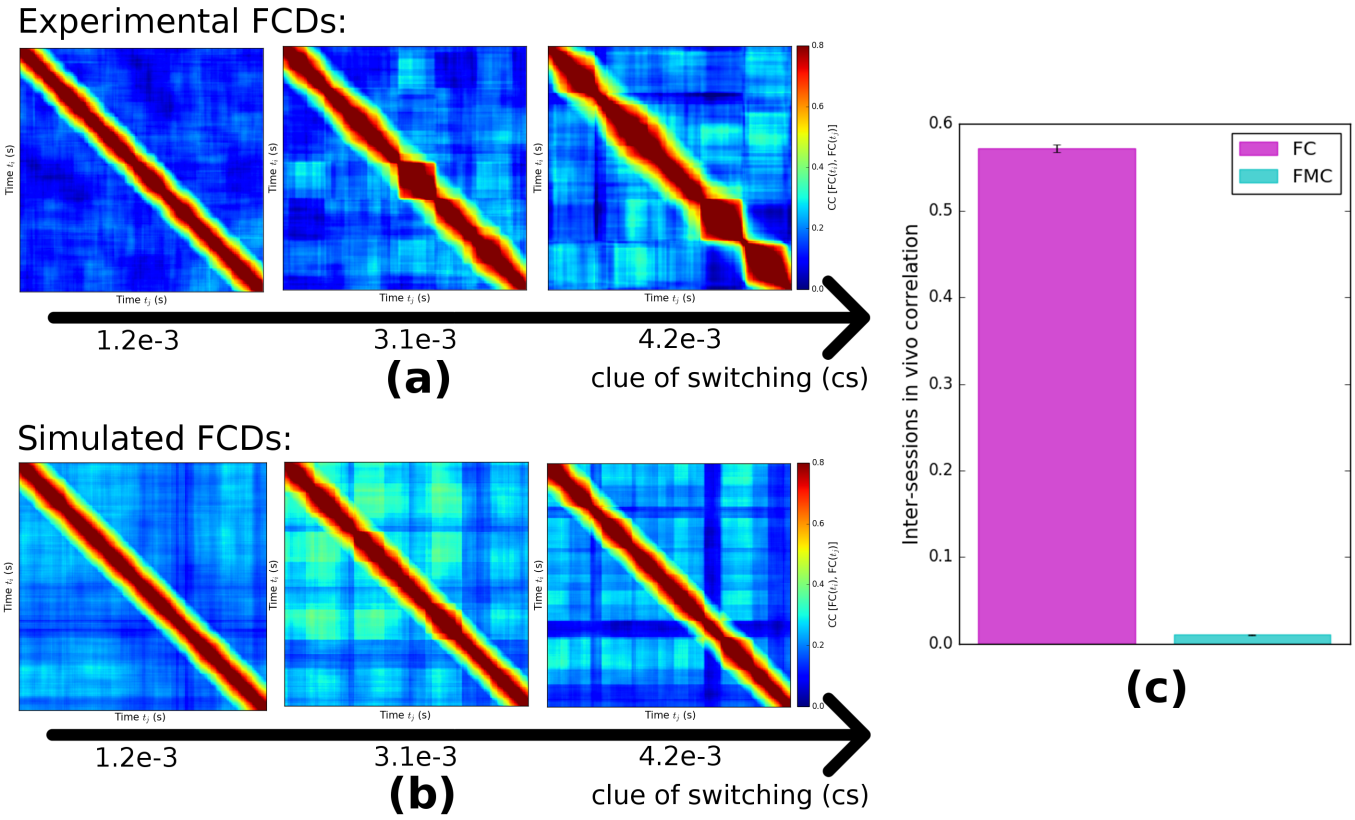

Figure S1: Variability of FCD metric in experimental (a) and simulated (b) data. FCDs on the top are calculated from the experimental resting state data from 3 different scanning sessions; FCDs on the bottom are calculated from simulated resting state data; in both case we use a sliding window length of 2 minutes and a spanning of 2.5 seconds. We quantify the presence of the switching, i.e. the checkboard pattern in the FCD matrix, as the variance of the triangular part of the FCD, once excluded the overlapping entries. We call this quantity: clue of switching (cs). The cs value is indicated below each FCD. FCDs are ordered for increasing cs values. The checkboard pattern appears more clearly as cs increases.

(c) The height of the bar represents the Pearson correlation between inter-sessions for experimental FC (magenta bar) and FMC (blue bar). The result shows that the FMC matrix can not be considered as a metric since FMC is poorly reproducible across sessions in the same animal.

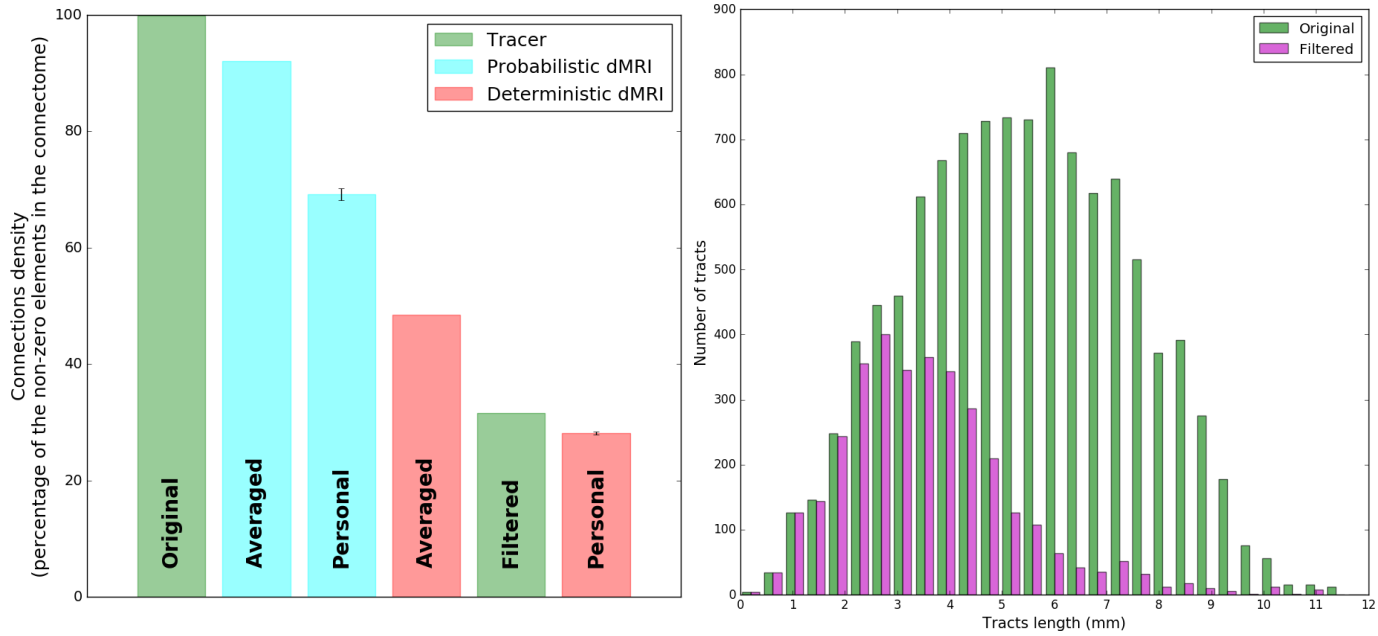

(a) (b)

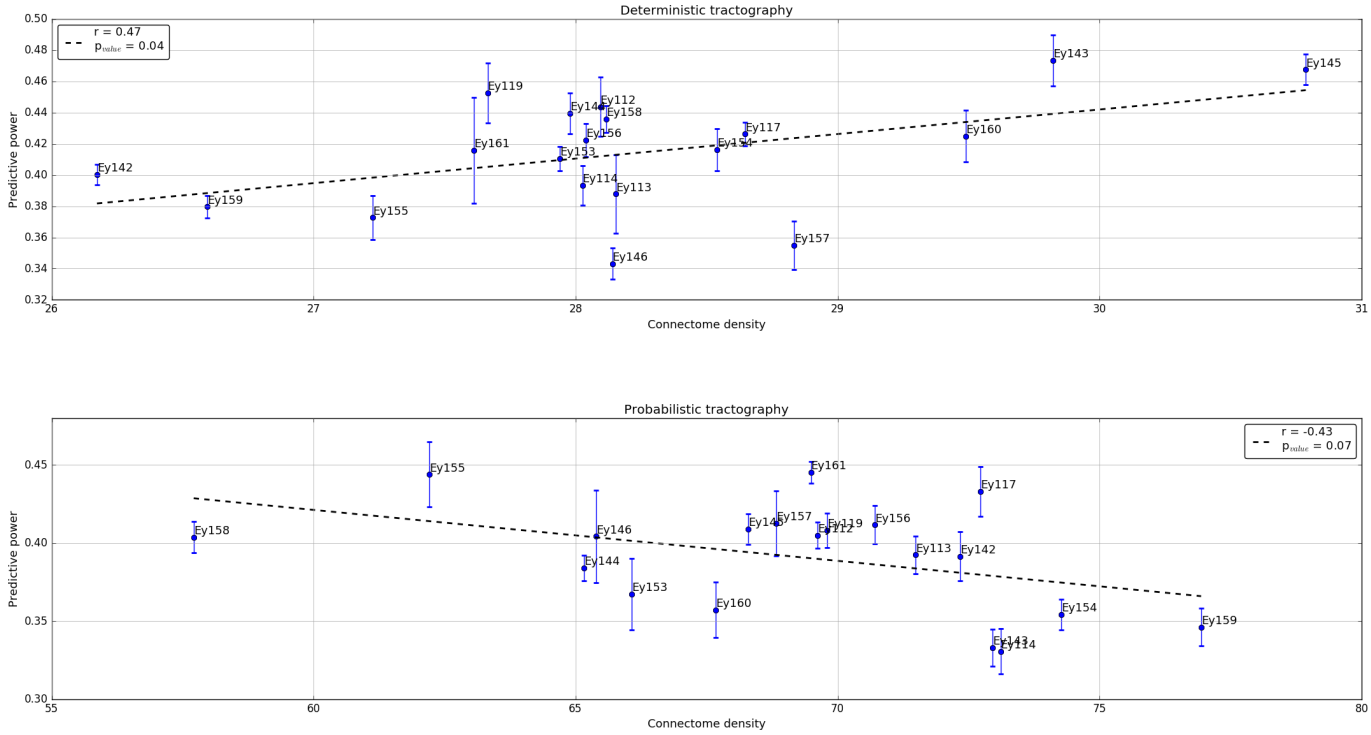

(c)

Figure S2

Figure S2: (a) The height of the bars represents the density of the connectome used in this study. The difference in the rank of the bars in this plot and those representing the connectomes PP (Figure 2-3) highlights the absence of a relation between the connectome's density and its PP. In line with this observation, the plots in (c) show the relation between the PP and the density of the dMRI-based connectomes processed with the deterministic tractography (plot on the top) and probabilistic tractography (plot in the bottom).The relation between the connectomes density and the PP it is opposite between the case of deterministic and probabilistic processing. In the case of deterministic processed tractography data, denser connectomes, i.e. with less false negative, have a greater PP than sparser connectomes, that is connectomes with more false negative. Conversely, in the case of probabilistic processed data, sparser connectomes, i.e. with less false negative, have a greater PP than denser connectome. From the results of the panels (a) and (c) it follows that the number of connections in a connectome does not directly relate with its ability in predicting brain dynamics.

The histogram in (b) shows the distribution of the fibers lengths included in the original tracer-based (green bars) and in the filtered tracer-based (magenta bars) connectome. The filtered connectome was obtained from the original tracer connectome by removing the connections not present in at least one of the 19 deterministic connectomes (68% of the tracer-based connections removed). This operation results in removing mainly long-range connections (the mean length of the tracts contained in the original tracer connectome and in the filtered one is respectively 5.40±0.02 mm and 3.57±0.03 mm).

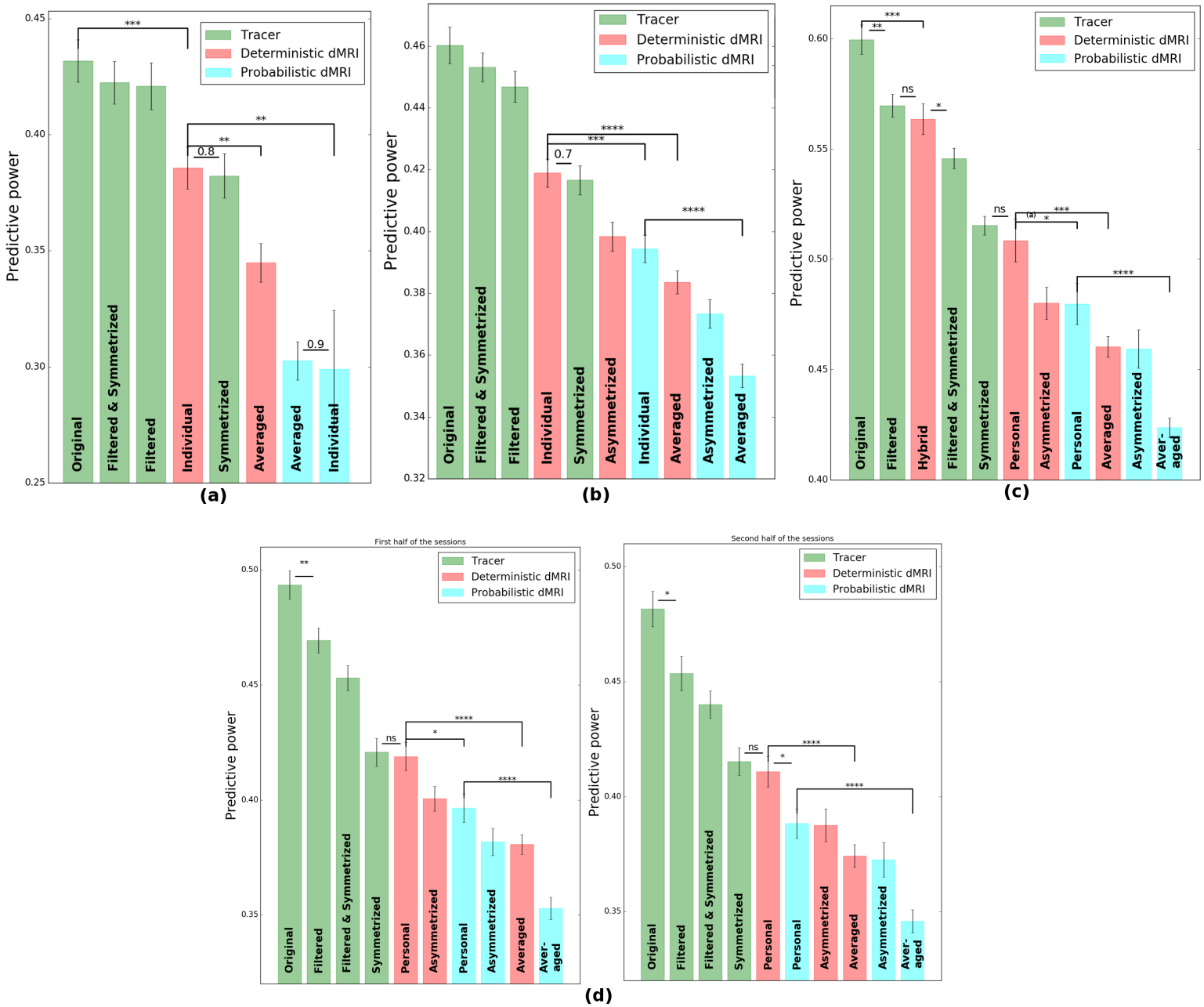
Predictive power
Tracer
Deterministic dMRI
Probabilistic dMRI
Original
Filtered & Symmetrized
Filtered
Individual
Symmetrized
Averaged
Asymmetrized
Hybrid
Personal
Aver-aged
(a)
(b)
(c)
First half of the sessions
Second half of the sessions
(d)

Figure S3:

Figure S3: The height of the bars in the plots represent the predictive power of the tracer-based (green bars), deterministic dMRI-based (red bars) and probabilistic dMRI-based (blue bars) connectomes. The meaning and the construction of the figures are analogous to Figure 3b 3C in the main text.

(a) Results obtained for examination of 7 wild type inbred C57BL/6 mice (4±2 sessions per animal, 11±4 minutes per session, mean±SD). The results are similar to those found for in hybrid mice.

(b) Results for hybrid mice obtained using experimental resting state data preprocessed using global signal regression. The results are consistent to those presented in Figure 2 and Figure 3, that are those obtained from experimental resting state data not not globally signals regressed.

(c) Results obtained after averaging recording sessions in the same animal. The predictive power trend is analogous to the one obtained considering separately the contribution of each recording session.

(d) The two bar plots show the predictive power calculated splitting the recoding sessions in two; results are consistent with the one obtained considering the complete dataset.

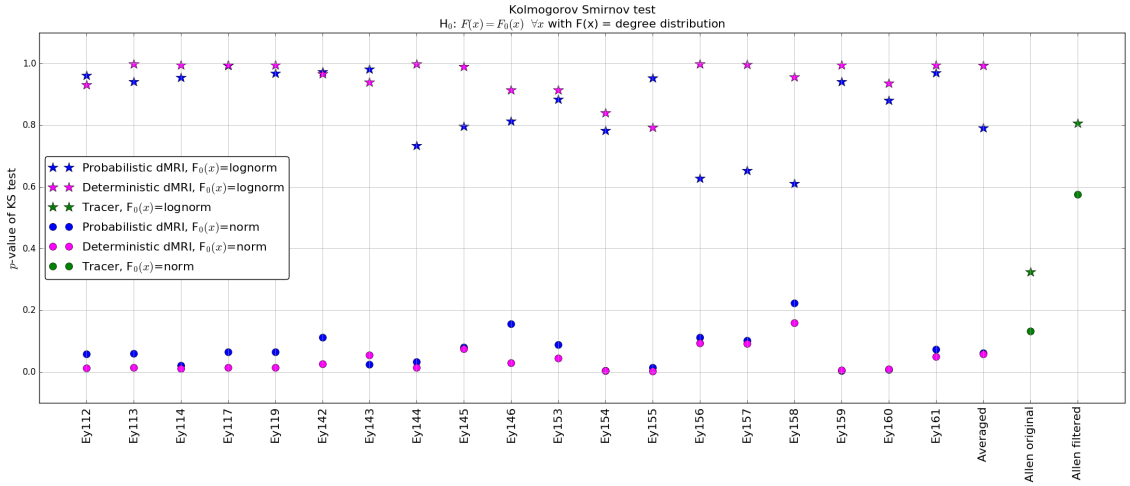

(a)

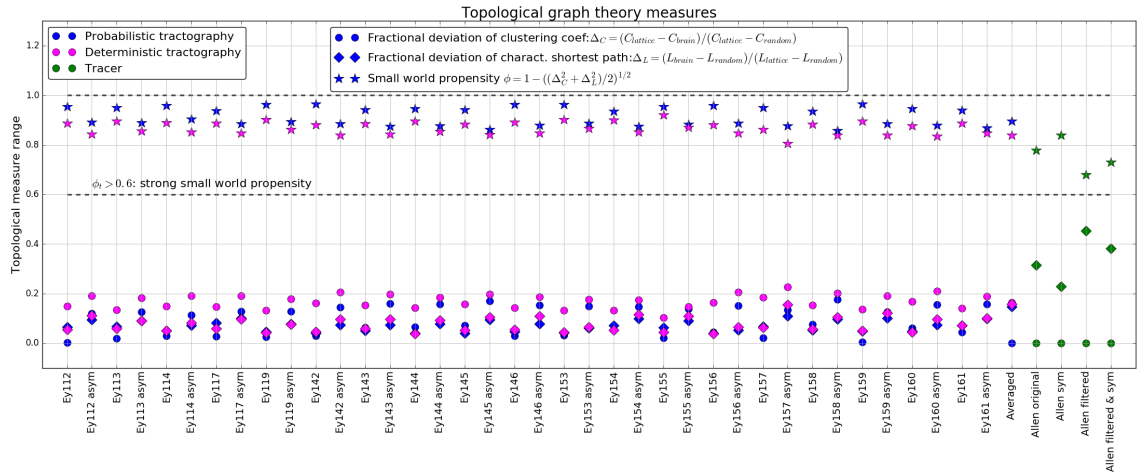

(b)

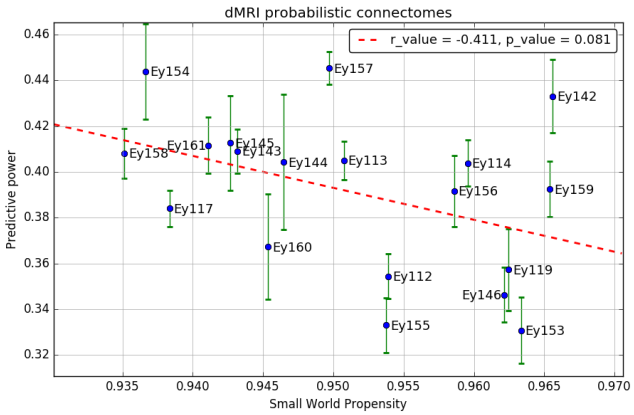

(c)

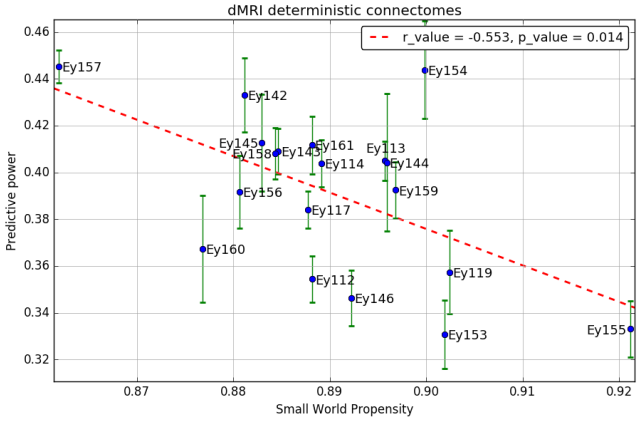

(d)

Figure S4

Figure S4: (a) The y-axis indicates the probability (Kolmogorov-Smirnov p-value) that the degree distribution of the connectomes shown on the x-axis come from a lognormal (star) or normal (bullet) distribution. Blue and magenta labels are for diffusion-MRI connectomes obtained with probabilistic and deterministic tractography respectively; green labels are for tracer-based connectomes.
(b) Topological measures calculated for all the connectomes used in this study (x-axis); blue, magenta and green labels are for connectomes obtained with, respectively, probabilistic dMRI, deterministic dMRI and tracer method. Bullet and diamond labels are the fractional deviations of the clustering coefficient and shortest path length, respectively, from their respective null mode (lattice and random, respectively). These values are used to define the Small World Propensity (SWP, star marker), for each graph. All connectomes have a SWP index above the threshold for small world topological structure ($\phi > 0.6$, Muldoon et al., 2016). Importantly, the tracer connectomes have a SWP index always smaller than that of the deterministic dMRI connectomes, which in turn have a SWP index always smaller than that of the probabilistic dMRI connectomes. Note that the relation between the SWP index of the different connectomes' families is exactly the inverse of the relation between the predictive power (PP) of the different connectomes' families: $SWP_{prob} > SWP_{det} > SWP_{tracer}$ and $PP_{prob} < PP_{det} < PP_{tracer}$.
(c) and (d) show the relation between the SWP and the predictive power of dMRI connectomes processed with probabilistic and deterministic tractography, respectively. Note the significant inverse linear relation between the SWP of a given deterministic dMRI connectome and its corresponding predictive power. In line with the previous observation (b), we can conclude that the more a connectome has a topological structure similar to the tracer one, the more reliable is the prediction of resting state dynamics.

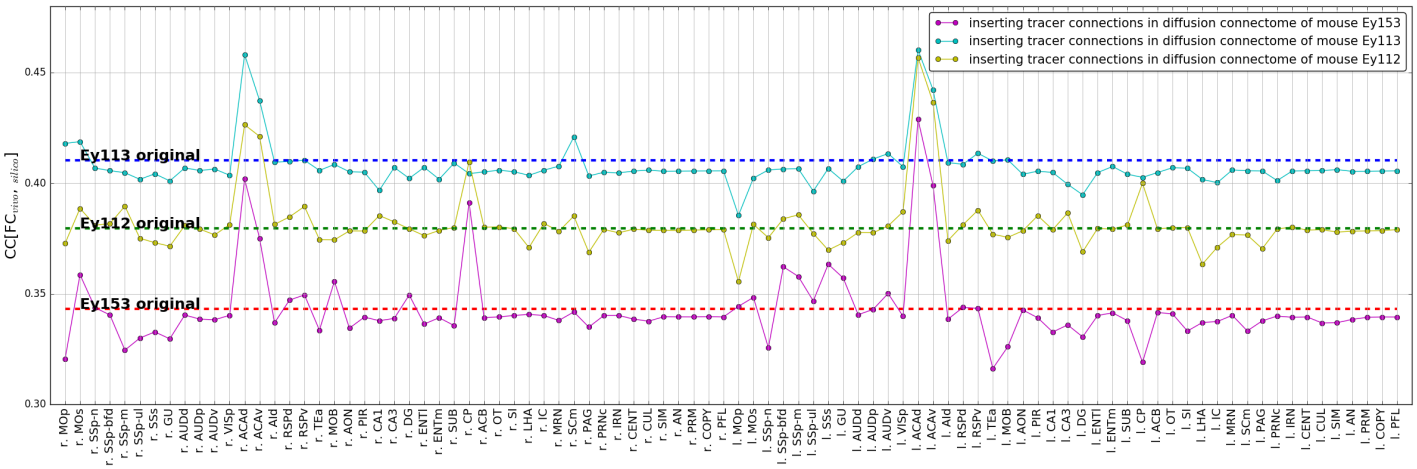

(a)

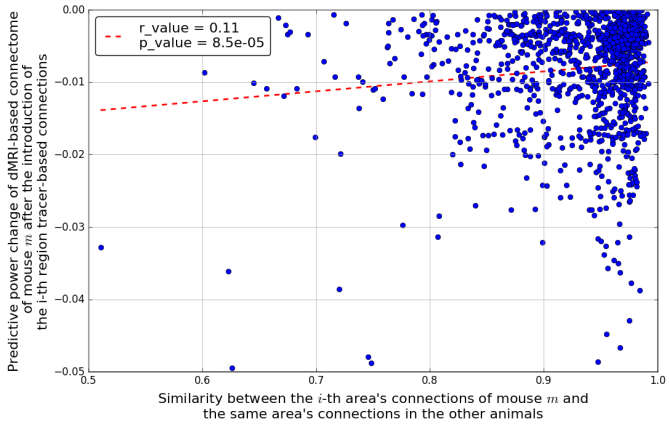

(b)

Figure S5: (a) Dots of different colors represent the predictive power of the deterministic dMRI connectome of different mice (namely Ey113, Ey112 and Ey153) with the connections of the brain area (x-axis) replaced with the corresponding tracer connections. Red, green and blue dashed lines represent the predictive power of the personal deterministic dMRI connectome of different mice. The figure shows that the change in predictive power strictly depends on the considered brain areas and on the mouse connectome: for example, the replacement of the right caudoputamen connections strongly enhances the predictive power of the deterministic dMRI connectome of mice Ey153 and Ey112, but not of mouse Ey113. Conversely, the replacement of cerebellum's connections does not really affect the performance of the connectome in predicting brain dynamics. The labels of brain areas are shown in table S1.
(b) The figure shows the relation between the peculiarity of the i-th brain area's deterministic dMRI-based connections of mouse m (x-axis) and the predictive power variation when the i-th area's tracer connections are added in the dMRI connectome of mouse m (y-axis).The peculiarity of the i-th area's connections of mouse m is quantified through the Pearson correlation between the connections under analysis and the corresponding ones of the other animals.

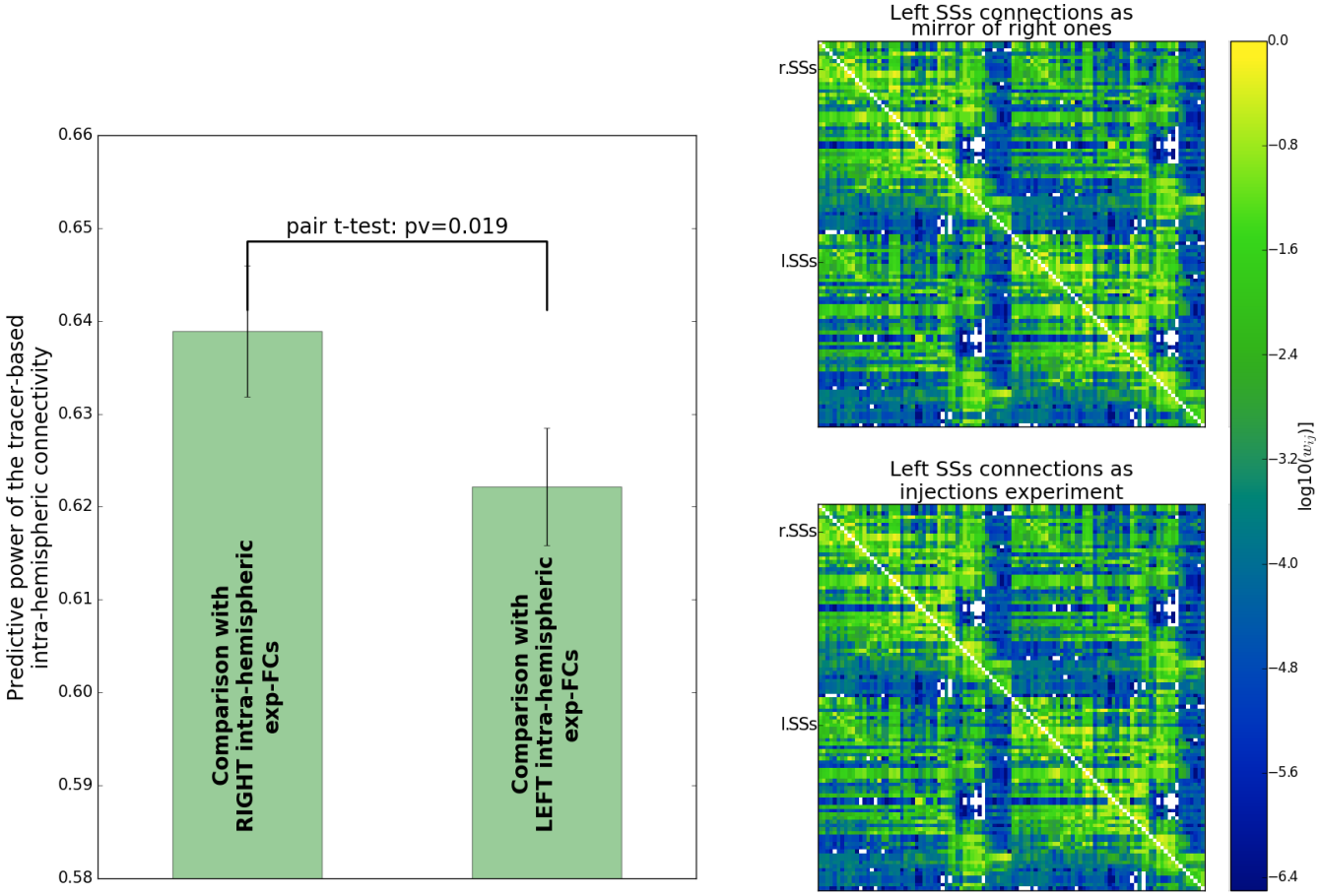

(a) (b)

Figure S6: (a)The height of the bars represent the predictive power of the tracer-based connectome built using only intra-hemispheric connections. The predictive power is estimated comparing the predictions of the connectome with the intra-hemispheric experimental functional connections measured from the right (left bar) or the left (right bar) hemisphere. The difference in the predictive power shows that intra-hemispheric tracer-based connections, obtained after injecting the compound in the right hemisphere, are able to predict better right than left intra-hemispheric functional connections. The result suggests that the mouse brain is lateralized.

(b) Tracer-based connectomes built using the information of one injection experiment per area. The difference between the two connectomes relies on the definition of the connections of the left SSs: in the connectome on the top, the connections of the left SSs are the mirror image of the connections of the right SSs, that are connections built using information from an injection experiment performed in the right SSs region. In contrast, in the connectome shown on the bottom, the left SSs connections are built using the information of an injection experiment performed in the left SSs area.